Magnetism and Spin Dynamics in Emergent Two-Dimensional van der Waals Magnets

by

Laith Alahmed

A thesis submitted to the Graduate Faculty of
Auburn University
in partial fulfillment of the
requirements for the Degree of
Master of Science

Auburn, Alabama
December 11, 2021

Keywords: 2D vdWs magnets, Magnetization Dynamics, FMR Spectroscopy

Approved by

Peng Li, Chair, Assistant Professor of Electrical and Computer Engineering
Michael Hamilton, James B. Davis Professor of Electrical and Computer Engineering
Masoud Mahjouri-Samani, Assistant Professor of Electrical and Computer Engineering

Abstract

The low Curie temperature of most two-dimensional (2D) van der Waals (vdWs) magnets makes it challenging to incorporate them into device applications. This thesis explores two intriguing materials: Fe_5GeTe_2, a 2D vdWs room temperature magnet, and Cu(1,3-bdc), a quasi-2D topological magnon insulator with low Curie temperature but peculiar magnetic properties. The materials were studied with various metrology, including X-ray diffraction, vibrating sample magnetometry, broadband FMR spectroscopy, thermal transport, etc. The magnetic measurements were performed with external magnetic fields applied in-plane and out-of-plane, and at different temperatures. We find that Fe_5GeTe_2 shows a record high Curie temperature of 332 K. Interestingly, for both magnets, a sizable Landé g-factor difference between the in-plane and out-of-plane cases was discovered, the Landé g-factor values deviate from $g = 2$, indicating a contribution of orbital angular momentum to the magnetic moment. The FMR measurements have revealed that Fe_5GeTe_2 has a damping constant comparable to Permalloy, and with reducing temperature, the linewidth has broadened. Our measurements not only demonstrate the room-temperature magnetization dynamics of Fe_5GeTe_2, but also provide evidence that Fe_5GeTe_2 transitions from ferromagnetic to ferrimagnetic at lower temperatures. In Cu(1,3-bdc), we have found that the interplay of topology, spin excitations, and orbital magnetism presents a playground for exploring topological spintronics. While the differences of in-plane and out-of-plane Landé g-factor (Δg) and saturation magnetization (ΔM_{s}) in Cu(1,3-bdc) are well correlated at low temperatures, they diverge at higher temperatures ($T >$ 4 K). Further theoretical analyses show that topological orbital moment induced by thermally excited spin chirality results in the g-factor anisotropy at higher temperatures. Our experiments have identified critical quantum phenomena in 2D magnets, highlighting them as ideal platforms for studying fundamental physics and building efficient spintronic devices.

Acknowledgments

I would like to sincerely thank Dr. Peng Li, for being the best advisor a graduate student could ask for. Without his constant support, patience, excellent mentorship, and kindness, none of my graduate achievements would have been possible.

I also thank Dr. Michael Hamilton and Dr. Masoud Mahjouri-Samani for serving on my committee and reviewing my thesis, and their groups for helping me with the sample preparation in the clean room.

My thanks extend to Dr. Luis Balicas, Dr. Matthew Brahlek, Dr. Brian Casas, Dr. Wencan Jin, Dr. Wai-Kwong Kwok, Dr. Young S. Lee, Dr. Yi Li, Dr. Alessandro R. Mazza, Dr. Claudia Mewes, Dr. Tim Mewes, Dr. Valentine Novosad, Dr. Jiajia Wen, Dr. Steven S.L. Zhang, Dr. Wei Zhang, Mr. Mr. Nicholas Jones, Mr. Juan Macy, Bhuwan Nepal, Mr. Arjun Sapkota, Ms. Yuzan Xiong, and Mr. Wenkai Zheng, for their great help in providing the raw materials, performing measurements, and discussions about data analysis and interpretation. Thanks and gratitude also go to Dr. Yuriy Mokrousov, Dr. Frank Freimuth, Mr. Li-chuan Zhang, and Mr. Fabian Lux, for helping in theoretical analysis and simulation.

Finally, a special thanks goes to my wife, Hadiah, for her unwaivering love and support, and for my family, including my father Abdulnaser, My mother Suzan, my sisters Hanan and Judy, and Osama, Nabeel, Yasmeen, and Ahmad, for always believing in me.

The work presented in this thesis is supported by the U.S. National Science Foundation (NSF) under grant No. DMR-2129879 and Auburn University Research Support Program.

Table of Contents

List of Figures

List of Tables

List of Abbreviations

$2D$	Two-Dimensional
$3D$	Three-Dimensional
bdc	Benzenedicarboxylate
CPW	Co-Planar Waveguide
DLT	Damping-Like Torque
DMI	Dzyaloshinskii-Moriya Interaction
FC	Field-Cooled
FCC	Field-Cooled Cooling
FCH	Field-Cooled Heating
FLT	Field-Like Torque
FMR	Ferromagnetic Resonance
$FWHM$	Full-Width-at-Half-Maximum
H_r	Resonance Field
IP	In-Plane
MFM	Magnetic Force Microscopy
OOP	Out-Of-Plane
$PPMS$	Physical Properties Measurement System

SSC	Scalar Spin Chirality
T_c	Curie Temperature
TOM	Topological Orbital Moment
$vdWs$	van der Waals
VNA	Vector Network Analyzer
VSM	Vibrating Sample Magnetometer
$XMCD$	X-Ray Magnetic Circular Dichorism
XRD	X-Ray Diffraction
YIG	Yttrium Iron Garnet
ZFC	Zero-Field Cooling

Chapter 1

Introduction

1.1 Background and Motivation

Magnetism is a phenomenon that fuels much of today's modern technologies. The complex mechanisms behind computer hard drives, data storage, non-volatile random access memory, medical equipment, telecommunication systems, and many other technologies, rely on magnetism, magnetic materials, and their unique and complex magnetic effects [1].

The microscopic origin behind magnetism stems from the magnetic dipole moments of individual electrons within a material [2]. Electrons not only carry negative charges, but they also have an intrinsic *spin* property. The spin of a free electron produces both angular momentum (due to its mass), and magnetic moment (due to its charge), along the spin axis. The magnetic moment of an electron is commonly referred to simply as the electron's spin. The direction of an electron's magnetic moment, or its spin (south pole, due to the electron's negative charge), is determined by the right-hand rule (see Figure 1.1).

If a long-range order of electron spins of unpaired electrons exists within a material, where the spins interact with each other and are collectively oriented in the same direction, then macro-scale magnetism emerges. Many factors affect the existence or the possibility of long-range magnetic order within materials, including material dependent properties, crystal structure, spin-orbit coupling, and thermal equilibrium. Some materials exhibit spontaneous long-range magnetic ordering under a certain temperature (known as the Curie temperature, T_c), while others require an external

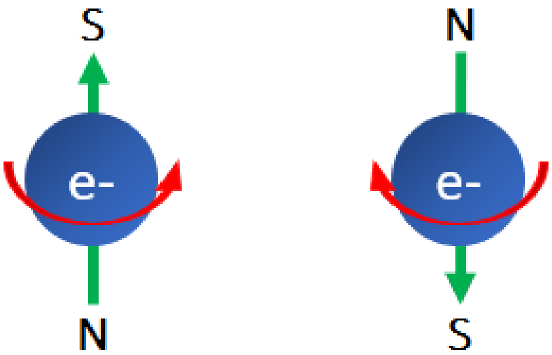

Figure 1.1: Electron spins. An electron spinning in the counterclockwise direction has a ”spin-up” magnetic moment direction. A clockwise spinning electron has a ”spin-down” magnetic moment direction.

magnetic field to induce the magnetic order, yet others are not affected by an external magnetic field and cannot be magnetized.

Based on their magnetic behavior, materials are usually separated into five different categories as follows [3]: 1) *Diamagnetism*: A fundamental, yet usually very weak, property of all matter. Diamagnetism arises from electrons resisting external magnetic fields. Diamagnetic substances have no net magnetization at zero external field, but produce negative magnetization when exposed to a field. 2) *paramagnetism*: A property of materials that have unpaired electrons that cannot interact with each other. Paramagnets, like diamagnets, have net zero magnetization at zero external field. When an external field is applied, however, the unpaired electrons can be influenced by the field, and they realign their spins to match the external field direction. This produces a net positive, yet very weak, magnetization. 3) *Ferromagnetism*: A property of materials possessing strong interactions between electron spins, resulting in parallel spins alignment and a large net magnetization, even in the absence of an external field. 4) *Ferrimagnetism*: A property similar to ferromagnetism, but the crystal structure of ferrimagnets is usually more complex, resulting in sublattices where the spins are oriented differently in each sublattice. 5) *Antiferrimagnetism*:

Another property similar to ferromagnetism, but the spins align themselves in an antiparallel fashion, rather than parallel.

Magnetism can exist in bulk materials or in two-dimensional (2D) structures, such as van der Waals (vdWs) ferromagnets [4]. Magnetism can also be observed in metals, semiconductors, as well as insulators, such as yttrium iron garnet (YIG) [5]. Because electrons are not usually free within a material, but orbit a nucleus, an orbital contribution to their angular momentum can be present. This so-called spin-orbit interaction can give rise to special effects such as the spin Hall effect, and magneto-crystalline anisotropy, where the spins prefer a certain direction, over any other.

From the above brief discussion, it is evident that magnetism and magnetic materials give host to a complex and diverse set of properties and mechanisms, including quasi-static magnetization properties and magnetization dynamics. In order to determine the usefulness and possible uses of a certain magnetic material, its magnetic properties must be characterized. Several methods employing a wide variety of equipment have been developed to do this. In this thesis, two unique 2D magnets are studied and characterized: a room-temperature 2D magnet Fe_5GeTe_2, and a topological magnon insulator Cu[1,3- benzenedicarboxylate(bdc)].

1.2 Research Progress of 2D Magnets

1.2.1 2D Magnets

The increasing interest in magnetic 2d van der Waals (vdWs) materials in recent years is warranted by their importance for fundamental studies of 2D magnetism, as well as potential applications for spintronic devices. Compared to three-dimensional (3D) magnets, 2D magnetic materials exhibit exotic electrotransport, optical, and spin properties.[6, 7, 8] One of the biggest practical issues of most 2D vdWs magnetic materials is that they generally have a Curie temperature (T_c) that is well below room temperature, making it difficult to incorporate them into relevant devices.[9, 10, 11, 12, 13, 14] For example, the Curie temperatures of 2D magnetic materials such as Cr(Si,Ge)Te_3 (33 K and 61 K)[9, 10], and Cr(Br,I)$_3$ (47 K and 61 K)[11, 12], are all lower than typical 3D magnets. This is due to their 2D nature, where the pair-exchange interaction is much weaker than in 3D magnets, as it is mostly mediated by neighboring magnetic atoms in the 2D plane.

The low T_{c} of the aforementioned 2D vdWs ferromagnets makes it impossible to use them in room-temperature spintronic devices. More specifically, in the 2D limit, it was shown theoretically that the Curie temperature is given by the uniaxial magnetic anisotropy constant K, and the spin-exchange interaction J, as follows[15]:

$$T_c \sim \frac{4\pi J}{3ln(\pi^2 J/K)} \tag{1.1}$$

According to Equation (1.2.1), as the magnetic anisotropy in vdWs ferromagnets is much smaller than the exchange interaction, T_{c} is low.[16] Extensive research efforts succeeded in engineering 2D materials that could overcome these challenges. For example, T_c can be significantly raised to about room temperature by enhancing exchange interaction while keeping the vdWs structure,[16] such as in the layered 2D Fe_nGeTe_2 ($n \geq 3$)[17, 18]. This led to Fe_3GeTe_2 with T_c around 220 K[19, 20, 14], Fe_4GeTe_2 with T_c = 270 K[16], and Fe_5GeTe_2 with T_{c} ranging from 260 - 310K, depending on the Fe content[18, 21, 22].

1.2.2 Room-Temperature 2D Magnet Fe_5GeTe_2

Fe_5GeTe_2 has arisen as a new member of vdW magnets following its cousin $Fe_{3-x}GeTe_2$[23]. Fe_5GeTe_2 has a complex atomic structure with multiple nonequivalent iron sites[21]. Its unit cell is composed of three Fe_5GeTe_2 layers with three non-equivalent Fe sites labeled as Fe(1), Fe(2), and Fe(3) in Figure 3.1a. Fe_5GeTe_2

has a structural phase transition at 570 K and the crystal structure depends on how the crystal is cooled down[21]. When Fe_5GeTe_2 is immediately cooled down after its growth in a furnace at around 1000 K, it is referred to as a quenched sample. The act of quenching was reported to reduce the broadening of the diffraction peaks significantly, which may be attributed to a stacking fault[21]. The change in stacking order is expected to be very subtle, leading to ambiguity in the crystal structure's point group. Stahl et al. reported a low symmetry group of $3\overline{m}$ for the naturally cooled sample[24]. However, May et al. demonstrated a high symmetry point group of $3m$ for the quenched sample[21]. So far, there are only several published transport studies on Fe_5GeTe_2[25, 26, 27]. Ref. [25] measured strong anomalous Hall effect in the Fe_5GeTe_2 thin film flakes (70 nm thick) as well as unique anisotropic magnetoresistance below 110 K. As shown in Figure 3.1b, two magnetic transitions are identified in the M-T curve: the first transition from ferromagnet to ferrimagnet at 275 K, and a second transition from ferrimagnet to a state with glassy clusters at 110 K. In another study, topological Hall effect-like features were measured in a Fe_5GeTe_2 flake, which was correlated to the unconventional (anti)meron chains observed in a Lorentz transmission electron microscope[26]. A third study demonstrated that the anomalous Hall curves are very sensitive to the layer numbers of the Fe_5GeTe_2 flakes. These prior works have suggested that the magnetic phase is strongly dependent on the temperature and the stack order of the Fe_5GeTe_2 flakes[27]. These studies used separate electrotransport and magnetic imaging measurements and have observed interesting physics. However, simultaneous measurements will be ideal for forming a correlated picture of magnetic texture and electrotransport features in Fe_5GeTe_2.

Fe_5GeTe_2 was first synthesized by May et al., who found that its Curie temperature is $\sim$ 310 K[21, 22]. It was later discovered that Fe_5GeTe_2 possesses itinerant long-range ferromagnetism[18], which originates from the giant spin polarization of the delocalized ligand Te states[28]. A recent work reported that Fe_5GeTe_2 transitions from ferromagnetic to ferrimagnetic at 275 K, and then to glassy clusters as the temperature reduces to 100 K [25]. Besides, several groups carried out electro-transport measurements and detected anomalous and topological Hall effects[25, 26, 27]. The magnetization dynamics in Fe_5GeTe_2, however remain unexplored, and thus is studied in this thesis.

While Fe_5GeTe_2 is one of the first room-temperature 2d vdWs magnets, the other material studied in this thesis is Cu(1,3-bdc), which has an extremely low T_c of around 1.8 K[29]. It is, however, a topological magnon insulator with peculiar magnetic behavior, and thus is selected as the second material for characterization.

1.2.3 Topological Magnon Insulator Cu(1,3-bdc)

The discovery of topologically protected states in some systems with fermionic particles (e.g. electrons and holes) led to extensive research efforts on topological insulators unraveling their unique properties[30]. Such topology-protected states can exist within the band gap of systems with bosonic quasi-particles as well, such as photons [31, 32], phonons [33] and magnons [34, 35, 36, 37, 38, 39], which can mediate the transport of spin and orbital angular momentum [40, 41, 42, 43]. While the interplay between the topology of electronic bands and spin transport properties has been intensively studied [44, 45, 46], the relationship between magnonic topology and intrinsic magnetic properties remains largely unexplored [36].

Non-trivial magnonic band topology was predicted in magnonic crystals such as $Lu_2V_2O_7$ and Cu(1,3-bdc) [34]. Cu(1,3-bdc) is a metal-organic hybrid material where the Cu^{2+} ions are arranged in a geometrically perfect Kagome lattice structure. The organic (1,3-bdc) molecules separate the individual Kagome planes, leading to weak interlayer interaction. It is thus identified as the first quasi-two-dimensional (2D) topological magnon insulator where strong exchange coupling is confined within individual layers [47]. Recent neutron scattering experiments identified the emergence of flat bands originating from the unique geometry of the Kagome lattice, which can be described by a Heisenberg Hamiltonian with Dzyaloshinskii-Moriya interaction [48, 29]. Thus, these exotic properties have made Cu(1,3-bdc) an ideal platform for exploring the interplay between magnonic topology and intrinsic magnetic properties including magnetization dynamics [49].

A recent theory has proposed that chiral magnetism and topological magnonic excitations can be correlated with electronic orbital magnetism [50, 51]. In particular, it is suggested that orbital magnetization can play a significant role in the dynamics of collinear antiferromagnets with weak spin-orbit coupling [50]. However, experimental evidence concerning the role of magnon-mediated electronic orbital moment in magnetization dynamics is still lacking. In this regard, it is crucial to carry out experiments to uncover the underlying physics on this topic.

Chapter 2

Experimental Techniques

2.1 Metrology of 2D Magnets

Table 2.1: Magnetic Properties and Characterization Techniques

Magnetic Property	**Characterization Technique**	**Equipment**
Effective magnetization Gyromagnetic ratio/g-factor Magnetic damping Resonance fields Inhomogeneous linewidth broadening	FMR	DynaCool PPMS
hysteresis loop Coercivity/remnant magnetization/Saturation fields Magnetic anisotropy Curie temperature	VSM	DynaCool PPMS
Magnetic phase transitions and Curie temperature	Heat Capacity	DynaCool PPMS
Magnetic domains/domain walls	MFM	Tosca 400

Some of the most important magnetic properties and their characterization techniques are summarized in Table 2.1.

2.1.1 Physical Properties Measurements System (PPMS)

A physical Properties Measurement System (PPMS), such as the DynaCool by Quantum Design USA, is an invaluable piece of equipment that comes with many options to characterize various physical properties, including magnetic properties. The DynaCool PPMS itself has two main features: it has a sample chamber with a controllable temperature that can span the range of 400 K to 1.6 K, and a superconducting magnet that can reach up to ± 9 T.

2.1.2 Heat Capacity Measurement

One of DynaCool's options is heat capacity, which measures the change in the thermal capacity of a sample (in Joules per Kelvin) with respect to a changing temperature. Heat capacity versus temperature plots can reveal magnetic phase transitions.

2.1.3 Vibrating Sample Magnetometry

Another important option that is compatible with the DynaCool PPMS is the Vibrating Sample Magnetometer (VSM). VSM measures the magnetic moment (in emu) of a sample as a function of an externally swept magnetic field, or as a function of temperature. Dividing the measured moment by the volume of the sample gives its magnetization, in units of emu/cm^3. Measurements of the moment versus field for a sample give its hysteresis loop. Hysteresis loops can be fitted to reveal many important magnetic properties, including: the saturation field required to saturate the magnetization of a sample, saturation moment (and in turn, saturation magnetization), the coercivity of a sample and its coercive field, which is the field required to completely demagnetize the sample, as well as the remnant magnetization of a sample when the external field is removed. Refer to Appendix A for more information on VSM data fitting. Measuring the hysteresis loops for two separate cases where the external field is applied out-of-plane (OOP), and in-plane (IP), respectively, can additionally reveal if the sample possesses magnetic anisotropy. This is done by comparing the saturation field required to saturate the magnetization of the sample in both cases. For example, if the saturation field when the field is applied IP is smaller than the saturation field when the field is applied OOP, then the sample exhibits IP anisotropy.

Measuring the magnetic moment versus temperature gives insight on the Curie temperature of the sample, which is the temperature above which thermal fluctuations dominate over the magnetic order of a sample, and the magnetization of the sample is lost [52]. Moment versus temperature measurements are usually performed in either of two conditions known as *zero-field cooling* (ZFC) and *field cooling* (FC) [53]. In the zero-field cooling case, the sample is cooled down in zero field from the high temperature point of interest T_{H}, to the low temperature point of interest T_{L}. Then, a small field, well below the saturation field of the sample (usually around 50 Oe), is applied, and the moment is measured as the temperature is increased from T_L to T_H, giving us the ZFC data. To get the FC data, the field is kept on, and then the moment is again measured while the temperature is lowered from T_H to T_L. The measurements can also be performed for a field applied IP or OOP, with results that could vary depending on the sample under test.

2.1.4 Magnetic Force Microscopy

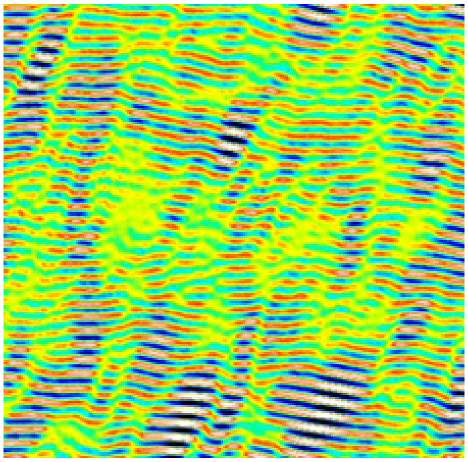

Figure 2.1: Magnetic domains in a 2D magnet $CrTe_2$ (Courtesy of Chunli Tang, unpublished)

In some ferromagnetic materials, the long-range magnetic order in one region, or domain, differs from a neighboring domain, where the domains are separated by what is known as a domain wall . Domain walls can produce skyrmions [54]. Magnetic domains and domain walls can be imaged by Magnetic-Force Microscopy (MFM). MFM can be performed through measurement devices such as the Tosca 400 Atomic Force Microscope from Anton Paar (see Figure 2.1).

2.1.5 Broadband Ferromagnetic Resonance (FMR) Spectroscopy

Broadband Ferromagnetic Resonance (FMR) spectroscopy, is another important technique that is especially useful for the characterization of Magnetization Dynamics. With FMR, one can extract the effective magnetization of a sample, its gyromagnetic ratio, its Gilbert magnetic damping constant, its resonance fields and frequencies, as well as many other important magnetic properties. Extensive details on broadband FMR spectroscopy can be found in Appendix B.

In the following two chapters, the various experimental setups and techniques discussed above are used to characterize the quasi-static magnetization properties and magnetization dynamics in Fe_5GeTe_2 and Cu(1,3-bdc).

Chapter 3

Magnetism and Spin Dynamics in Room-Temperature van der Waals Magnet Fe_5GeTe_2

3.1 Introduction

In this chapter, the magnetic properties of 2D vdWs Fe_5GeTe_2 bulk crystals are studied. First, vdWs magnet Fe_5GeTe_2 was synthesized, and then its magnetization properties were studied using both VSM and FMR spectroscopy, in the temperature range of 300 K to 10 K. For FMR, a microwave field was applied to the sample in addition to a quasistatic magnetic field, thus triggering spin precession. At the resonance field H_{res} for a given microwave frequency f, FMR oscillations (uniform-mode excitation with $k \approx 0$) occur. The FMR spectroscopy has revealed different Landé g-factors along the c-axis and the ab-plane in Fe_5GeTe_2, indicative of orbital moment contribution to the magnetic moment. After examining the temperature dependence of the FMR linewidth, the results show that Fe_5GeTe_2 has an effective damping coefficient similar to Permalloy at room temperature. The increased FMR linewidth at lower temperatures indicates that Fe_5GeTe_2 experiences a magnetic phase transition from ferromagnetism to ferrimagnetism.

3.2 Structural Characterization

Nominal Fe_5GeTe_2 crystals were grown at the National High Magnetic Field Laboratory using a mixture of precursor materials filled into a quartz ampoule that is vacuumed and sealed with 1.9 mg/cm^3 of iodine as a transport agent. The mixture consists of pure elements of Fe:Ge:Te in the molar ratio of 6.2:1:2 (Fe: 99.998%, powder, Alfa Aesar; Ge: 99.999%, 100 mesh, Alfa Aesar; Te: 99.999%, powder, Alfa Aesar). The excess Fe powder is to compensate for any possible Fe-site vacancies that might occur during the growth.

A standard MTI 2-zone model OTF-1200X furnace was employed, where the reactants or elemental precursors were placed in the high-temperature zone and the products were grown in the low-temperature side. The ramping rate for both the hot (775 °C) and cold (700 °C) zones to their target temperatures was 1 °C/min. This temperature differential was held for 14 days with the Fe_5GeTe_2 crystals being subsequently quenched in an ice bath.

Prior to characterization, the excess iodine was removed through a bath and rinse cycle of acetone and isopropyl alcohol, respectively. Samples were either stored in a glove box with high purity argon gas (99.99%) of 0.01 ppm O_2/H_2O, or a desiccator under vacuum with pressures ranging between 100-200 mTorr.

The following results are obtained from a bulk Fe_5GeTe_2 crystal in the shape of an ellipse, with area = 3.2×10^{-3} cm^2 and thickness $\sim$ 100 microns. The crystalline structure characterization is presented in Figure 3.1. Figure 3.1a shows the crystal structure schematic of Fe_5GeTe_2. The vdW-separated eight atomic-thick monolayers of two unit cells can be observed, where the vdWs gaps exist between the Te atoms of neighboring unit cells. The light-blue circles labeled Fe(1) represent the two possible occupation locations for the Fe(1) atoms, either above or below a given Ge atom, with an occupation probability not exceeding 50%, as the Fe-Ge bond becomes non-physical if both locations are occupied simultaneously[21].

The X-ray diffraction (XRD) data collected for the experimental Fe_5GeTe_2 sample crystal are shown in Figure 3.1b. The $(00l)$ reflections reveal the c-axis of the single crystal. The $(00l)$ peaks, where l=3n, reflect an ABC stacking sequence in the unit cell of the bulk crystal. This is consistent with the rhombohedral lattice structure of the R3m (No. 166) space group, as previously reported[21, 18].

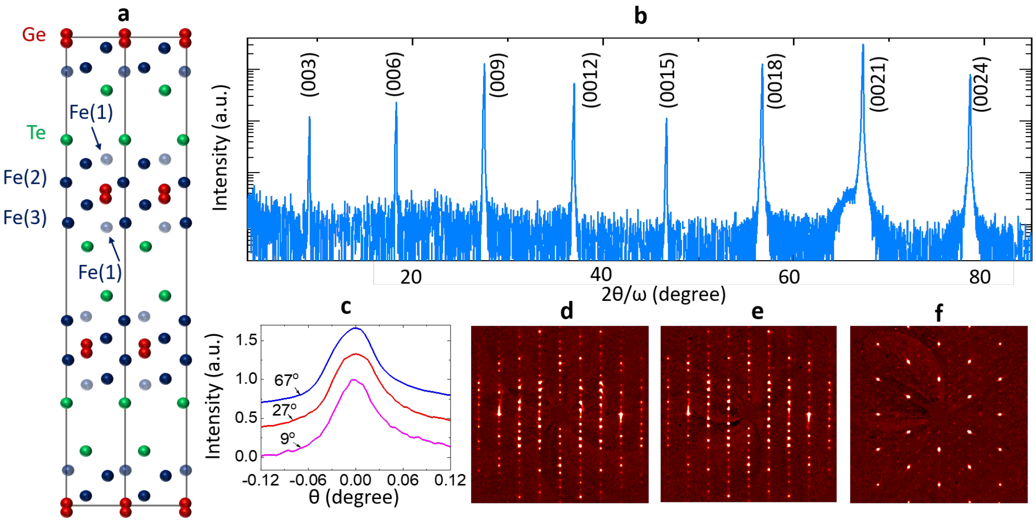

Figure 3.1: Crystal structure and x-ray diffraction (XRD) of single crystal Fe_5GeTe_2.[55] **a**. Schematic of crystal structure of Fe_5GeTe_2. **b**. XRD $2\theta/\omega$ scan showing $(00l)$ peaks. **c**. Rocking curve scan of the peaks at 9°, 27°, 67° showing high crystallinity. **d-f**: Single crystal XRD scan of Bragg reflections of different planes. **d**: $(0kl)$ plane. **e**: $(h0l)$ plane. **f**: $(hk0)$ plane.

The rocking curves measured at $(00l)$ peak angles are shown in Figure 3.1c. The full-width-at-half-maximum values of the acquired curves, with values less than 0.06^{o}, reflect the high level of crystallinity of the Fe_5GeTe_2 samples. Figures 1d-f are Bragg reflection scans of different crystal planes $(0kl)$, $(h0l)$, $(hk0)$ from high-resolution XRD. They all show clear streaks, confirming the high-quality of the single-crystal samples.

3.3 Quasi-Static Magnetization Properties

Quasi-static magnetization properties were measured using VSM in a Quantum Design Dynacool PPMS system. The measurements were carried out with the magnetic field applied along both the c-axis ($H\|c$) and the ab-plane ($H\|ab$) directions. To determine the Curie temperature of the sample, field-cooled curves were measured, as well as heat capacity curves in the absence of a magnetic field.

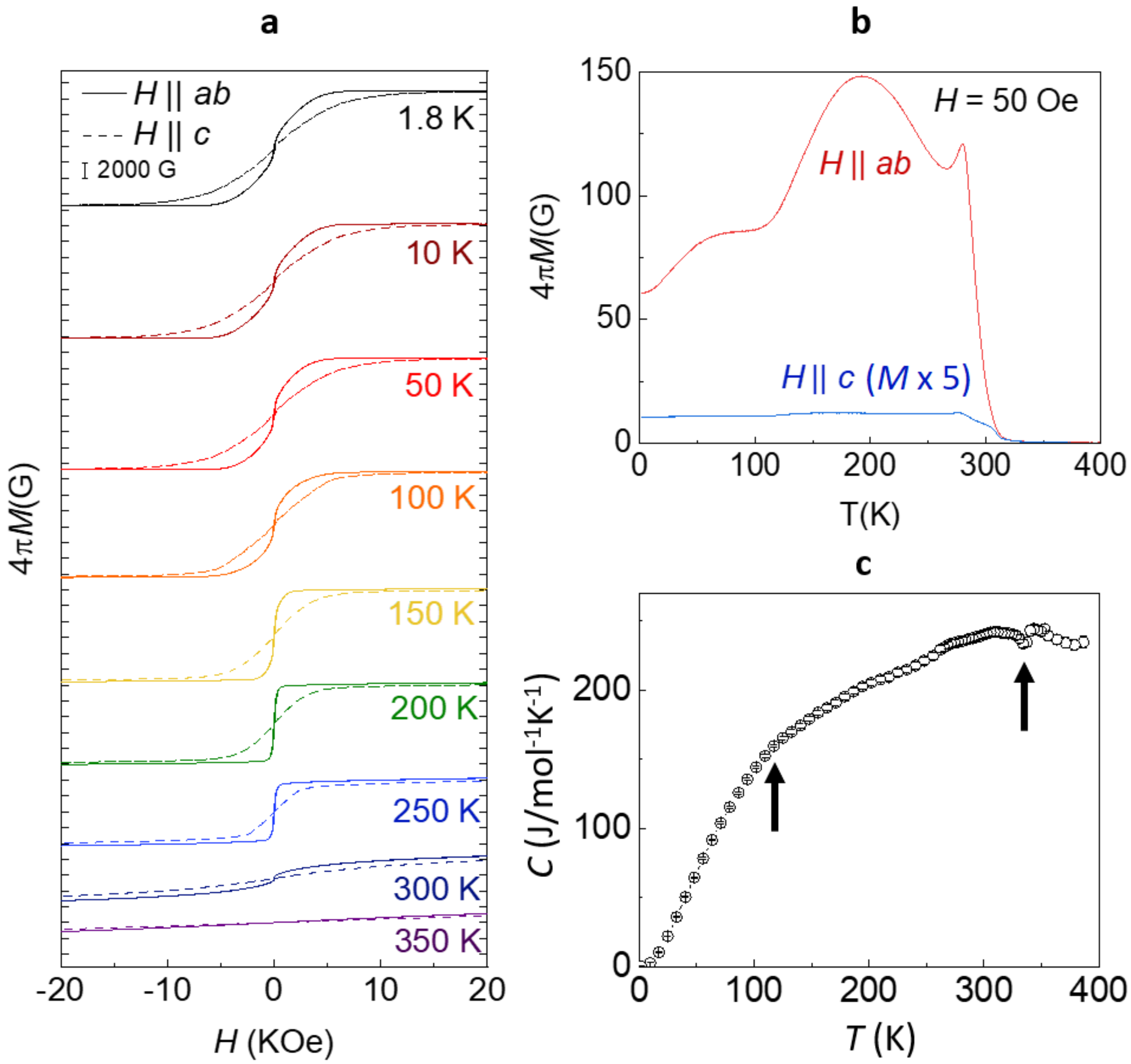

Figure 3.2: Static magnetization of the Fe_5GeTe_2 bulk single crystal.[55] **a**. Temperature-dependent hysteresis loops at various temperatures for $H\|c$ (dashed lines) and $H\|ab$ (solid lines). **b**. Field-cooled curves ($H = 50$ Oe) for the $H\|c$ (blue) and the $H\|ab$ (red) cases, respectively. **c**. Heat capacity as a function of temperature. The transition at 332 K and 110 K mark the Curie temperature and possible magnetic phase transition, respectively.

Figure 3.2a shows the results of the VSM magnetization versus field measurements of the Fe_5GeTe_2 sample, for temperatures ranging from 1.8 K to 350 K, and external field applied along both the c-axis (dashed lines) and the ab-plane (solid lines) directions. The curves show that the easy-axis of Fe_5GeTe_2 is IP because a stronger field is required to saturate the sample along the c-axis, compared to the *ab*-plane, at all temperatures. Possible spin-reorientation features, such as the ones observed in Fe_4GeTe_2 [16], are not observed in this sample. The results are reasonable considering the fact that the OOP magnetocrystalline anisotropy in Fe_5GeTe_2 crystals is weak. [25, 16]. Figure 3.2b shows the field-cooled (FC) curves for the $H\|c$ and the $H\|ab$ cases. The magnetization magnitude change on the $H\|ab$ curve indicates a possible magnetic phase transition. This feature has been reported in previous publications [16, 25, 21]. Based on the transition points of the FC curves, the Curie temperature was estimated to be $T_\mathrm{c} = 332 \pm 5$ K.

Heat capacity measurements were used to validate the Curie temperature estimation. The measurements were set to start from the highest temperature setpoint, $T = 390$ K, then the temperature was gradually reduced to 1.8 K as the heat capacity data was collected. This procedure guarantees that an appropriate time constant is used to achieve more stable readings. The measurement results are shown in Figure 3.2c. Two points of interest are highlighted on the curve by two black arrows. The first is a transition at $T = 332$ K, which is consistent with T_c from the FC measurement. The second is the observation of a slope change around $T = 110$ K. The slope change again indicates that Fe_5GeTe_2 experiences some phase transition, which will be discussed more extensively in the analysis of FMR linewidth in Section 3.4.

In order to determine whether there is any crystalline anisotropy present IP, VSM magnetization hysteresis loop measurements were carried out along different IP axes, as shown in Figure 3.3.

Figure 3.3 shows the hysteresis loops measured along different IP axes at 1.8 K, 100 K, 200 K and 300 K. The Fe_5GeTe_2 crystal was first measured at 0^o at different temperatures. Then, the Fe_5GeTe_2 crystal was rotated clockwise to 90^o and 120 ^{o} with respect to the initial axis of the Fe_5GeTe_2 crystal and measured at the same temperatures. At all temperatures, the hysteresis loops do not show any significant

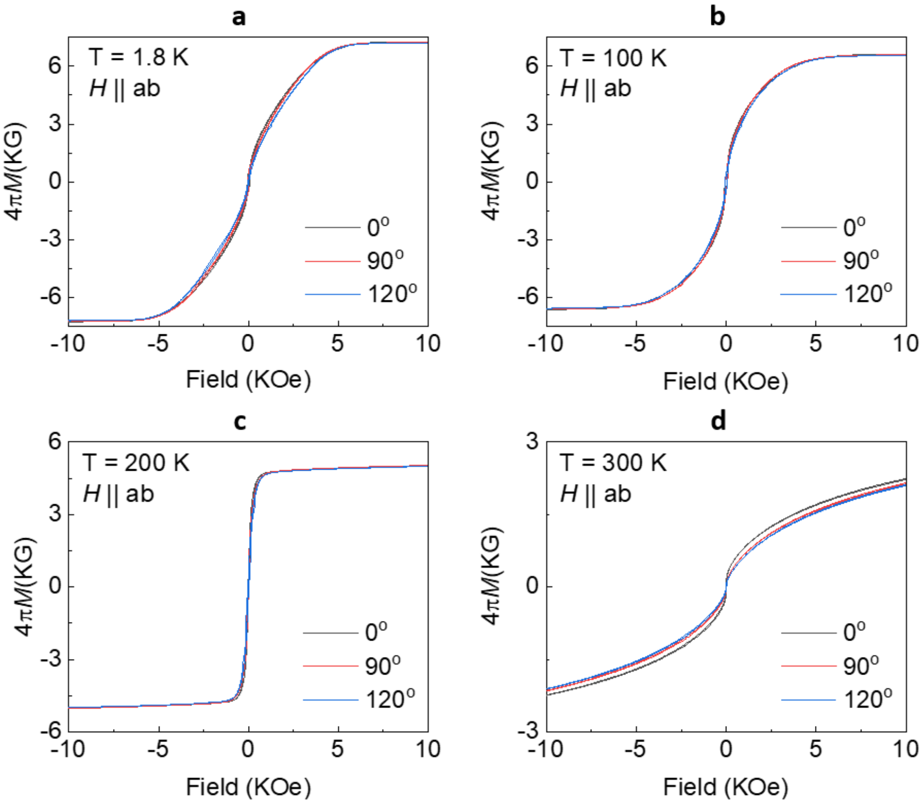

Figure 3.3: Angle-dependent hysteresis loops for $H\|ab$ at different temperatures.[55] **a** 1.8K, **b** 100K, **c** 200K, and **d** 300K

differences for the different angles, indicating that Fe_5GeTe_2 is an easy-plane magnet with no IP uniaxial anisotropy.

3.4 Magnetization Dynamics

The FMR response of the Fe_5GeTe_2 sample was measured for $H\|c$ and for $H\|ab$, at temperatures varying from 10 K to 300 K. In our custom-built system, a coplanar waveguide (CPW) with impedance matched to 50 Ω was used to guide the microwave field to the sample. The tested microwave frequencies ranged from 5 GHz to 40 GHz, with higher frequencies up to 115 GHz used in the room temperature $H\|c$ case, along with high magnetic fields, to ensure that the magnetization of the sample is fully saturated at FMR. For each microwave frequency, the magnetic field was swept from high magnetic field towards zero. A microwave diode was used to convert the

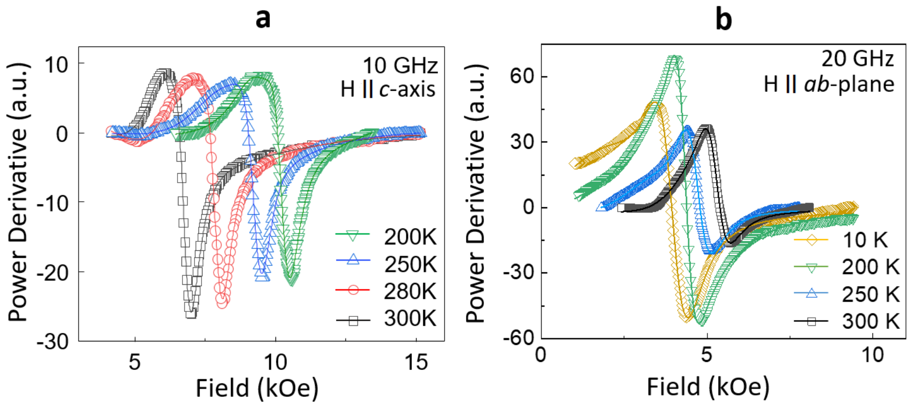

Figure 3.4: Ferromagnetic resonance (FMR) measurements of Fe_5GeTe_2 single crystal.[55] **a**. FMR profiles for $H\|c$ at 200 K, 250 K, 280 K, and 300 K. **b**. FMR profiles for $H\|ab$ at 10 K, 200 K, 250 K and 300 K.

transmitted microwave signal to a dc voltage. To improve the signal-to-noise ratio, a set of field-modulation coils supplemented by a lock-in amplifier to detect the signal were used. Thus, the detected FMR response is identified as the derivative of the microwave power absorption.

As shown in Figure 3.4, strong FMR responses are detected at 300 K, demonstrating ferromagnetism of Fe_5GeTe_2 at room temperature. Figures 3.4a and 3.4b show the temperature dependence of the FMR profiles at 10 GHz and 20 GHz, for $H\|c$ and $H\|ab$, respectively. Besides the data points, the curves show fits to the derivative of a combination of symmetric and antisymmetric Lorentzian functions[56]. The measured FMR response is a time-averaged signal of the microwave power absorption. Such absorption is dispersive and has a symmetric feature. However, there are a number of effects, including Eddy currents, that can lead to a phase shift of the driving microwave field relative to the original signal[57]. Such a phase shift leads to a quadrature component that manifests as an antisymmetric contribution to the FMR signal.[58, 59] From the fits, one can extract the resonance field H_r and peak-to-peak linewidth ΔH_{pp} as shown in Figures 3.5 and 3.7, respectively. It is observed that the magnitude of the FMR peaks decays with reducing temperature in the $H\|c$

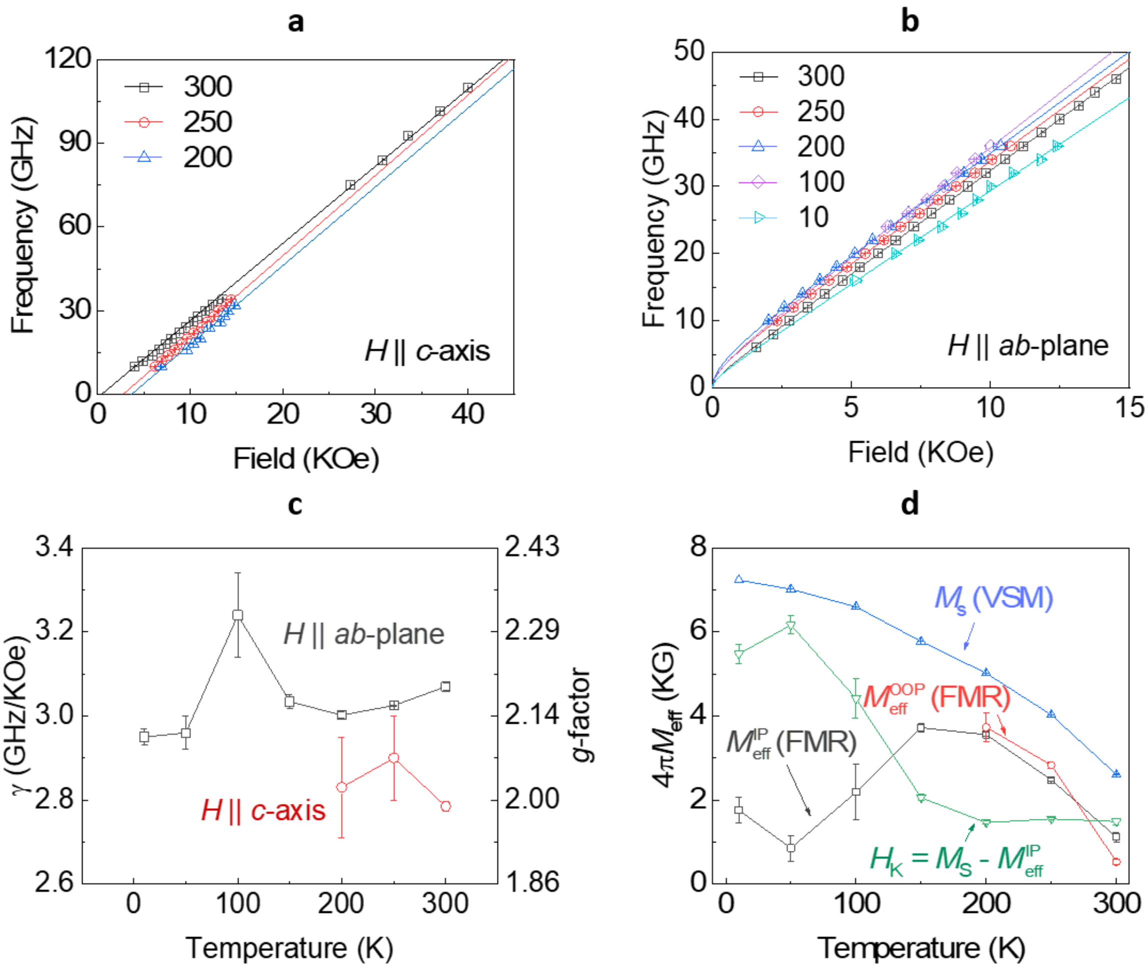

Figure 3.5: Analysis of the FMR data of the Fe_5GeTe_2 single crystal.[55] **a**. Frequency f vs. resonance field H_r at 200 K, 250 K, and 300 K for $H\|c$. The data points are fitted to Eq. 3.1. **b**. Frequency f vs. resonance field H_r at 10 K, 100 K, 200 K, 250 K, and 300 K for $H\|ab$. The data points are fitted to Eq. 3.2. **c**. Temperature dependence of the gyromagnetic ratio γ and spectroscopic g-factor for the $H\|c$ (red) and $H\|ab$ (black) cases, respectively. **d**. Temperature dependence of saturation magnetization $4\pi M_s$ and effective magnetization $4\pi M_{eff}$ from VSM and FMR measurements, respectively.

case. Below 200 K, the FMR signal becomes undetectable in this orientation. This phenomenon can be attributed to the broadening of the FMR resonance peaks.

The resonance frequencies f vs. the FMR resonance fields H_{r} at different temperatures are plotted in Figures 3.5a and 3.5b for the $H\|c$ and for the $H\|ab$ cases, respectively. The fitting equation for the $H\|c$ measurements is:[60]

$$f = \gamma'(H_r - 4\pi M_{\text{eff}}) \tag{3.1}$$

and the fitting equation for the $H\|ab$-plane measurements is:[60]

$$f = \gamma'\sqrt{(H_r + 4\pi M_{\text{eff}})H_r} \tag{3.2}$$

where f is frequency, γ' is the reduced gyromagnetic ratio ($\gamma' = \frac{|\gamma|}{2\pi}$), and $4\pi M_{\text{eff}}$ is the effective magnetization. The fitted curves are also presented in Figures 4a and 4b. By fitting the data with equations (1) and (2), one obtains different γ' and corresponding spectroscopic Landé g-factor values, as well as M_{eff} values, for the $H\|c$ and $H\|ab$ cases, as shown in Figures 3.5c and 3.5d, respectively. Note that the $4\pi M_{\text{eff}}$ values obtained along those two orientations are in good agreement with each other. A difference between these two values could be an indication for the presence of a higher order anisotropy [61], but this is not the case here.

In Figure 3.5c, the left vertical axis shows γ', and the right vertical axis shows the Landé g-factor calculated using $|\gamma| = g\frac{\mu_{\text{B}}}{\hbar}$. The g-factor exhibits a weak dependence on temperature along both the ab-plane and the c-axis directions. However, it deviates from $g = 2$.

Furthermore, our data appears to indicate a sizable difference of the g-factor along different directions in Fe_5GeTe_2. Similar to $Cr_2Ge_2Te_6$,[62] the deviation of the g-factor from $g = 2$ may suggest an orbital contribution to the magnetization due to spin-orbit coupling in Fe_5GeTe_2. It was found that strong spin-orbit coupling results in nontrival Berry phase in Fe_3GeTe_2, another member in the Fe_nGeTe_2 ($n \geq 3$) family. In this case, the orbital character is formed by a mixture of 3D orbitals from the Fe I–Fe I dumbbells and Fe II sites[63]. A theoretical work found that the magnons can have long lifetimes and exhibit nonreciprocal magnon transport in Fe_3GeTe_2.[64] In

Fe_5GeTe_2, the spin-orbit coupling could be characterized by the d orbitals of Fe atoms and p orbitals of Te atoms [62]. In addition, the anisotropy of the g-factor, which follows from that of the orbital moment, is also expected physically: a small orbital moment arising from reduced crystalline symmetry may "lock" the large isotropic spin moment into its favorable lattice orientation through spin-orbit coupling, giving rise to a sizable magnetic anisotropy. Therefore, it is likely that the orbital moment is closely linked to the magnetocrystalline anisotropy in itinerant ferromagnets, as shown theoretically by Bruno et al.[65] for transition-metal monolayers. A recent experiment used x-ray magnetic circular dichroism (XMCD) and detected the contribution of the orbital moment to the overall magnetization of Fe_5GeTe_2.[28]

It is worth noting that an unsaturated magnetization at FMR can also lead to an inaccurate estimation of the gyromagnetic ratio.[66] Because the c-axis magnetization saturates at significantly larger magnetic fields, it is possible that the magnetization was not fully saturated for FMR measurements up to 40 GHz. To estimate to first order the influence of an unsaturated sample at resonance, one can write $4\pi M_{\mathrm{eff}}(H) = 4\pi M_{\mathrm{eff},0} + 4\pi pH$, where H is the external field, $4\pi M_{\mathrm{eff},0}$ is the effective magnetization extrapolated to zero field, and $4\pi p$ is the slope of $4\pi M_{\mathrm{eff}}$ vs. H curve in the region where FMR occurs. Using this equation, equation 3.1 can be written as: $f = \gamma'_{\mathrm{meas}}(H_r - 4\pi M_{\mathrm{eff,meas}})$, with $\gamma'_{\mathrm{meas}} = \gamma'(1 - 4\pi p)$ and $4\pi M_{\mathrm{eff,meas}} = \frac{4\pi M_{\mathrm{eff}}}{1-4\pi p}$.

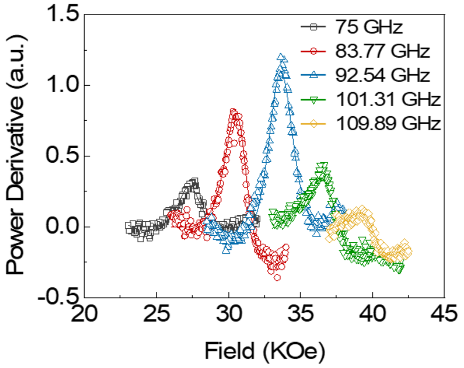

Figure 3.6: High-Field FMR measurements of Fe_5GeTe_2 single crystal at room temperature for the $H \| c$ case, at different microwave frequencies.[55]

To exclude this possibility and to comfirm the g-factor anisotropy, a setup with microwave frequencies ranging from 75 GHz to 110 GHz was used to excite FMR in $\mathrm{Fe_5GeTe_2}$ at room temperature. At these frequencies, the FMR resonance fields are between 25 KOe and 45 KOe, thus, ensuring the magnetization of the $\mathrm{Fe_5GeTe_2}$ crystal is fully saturated. The measured FMR responses are shown in Figure 3.6. The resulting g-factor extracted from the high-field FMR data still shows significant difference between the ab-plane and c-axis, as shown in Figure 3.5c. Thus, supporting the presence of a g-factor anisotropy in $\mathrm{Fe_5GeTe_2}$.

The fits also yield the effective magnetization $4\pi M_{\mathrm{eff}}$ at different temperatures. Figure 3.5d plots $4\pi M_{\mathrm{eff}}$ for both $H\|c$ (i.e., $4\pi M_{\mathrm{eff}}^{H\|c}$) and $H\|ab$ (i.e., $4\pi M_{\mathrm{eff}}^{H\|ab}$) cases measured from FMR, along with the saturation magnetization $4\pi M_{\mathrm{s}}$ measured from VSM. One can see (1) $4\pi M_{\mathrm{eff}}^{H\|c}$ and $4\pi M_{\mathrm{eff}}^{H\|ab}$ are close, and (2) there is a difference between $4\pi M_{\mathrm{s}}$ and $4\pi M_{\mathrm{eff}}$. This reveals a crystalline anisotropy field that can be calculated by $H_{\mathrm{k}} = 4\pi M_{\mathrm{s}}$ - $4\pi M_{\mathrm{eff}}^{H\|ab}$. As plotted in Figure 4d, H_{k} is positive and reduces with increasing temperature. This shows that there exists an OOP crystalline anisotropy field H_{k} of several kOe, though it is smaller than the IP shape anisotropy. This observation is consistent with previous reports.[25, 16]

Next, the FMR linewidth is analyzed in order to gain insights on the spin scattering mechanisms in $\mathrm{Fe_5GeTe_2}$. In Figures 3.7a and 3.7c, the peak-to-peak linewidth ΔH_{pp} vs. frequency is plotted at different temperatures measured for the $H\|ab$ and the $H\|c$ cases, respectively. For an ideal magnetic thin film that is homogeneous and defect-free, the linewidth reflects intrinsic FMR damping. In this scenario, the uniform magnon mode (k = 0, ferromagnetic resonance) decays into Stoner excitations as temperature decreases. This involves the transition of an electron from an occupied state to an unoccupied state of the same wave-vector, which can be described by the interband term in Kambersky's formula[67, 68]. It should be noted that Kambersky's model is only appropriate to second order in spin-orbit coupling parameter

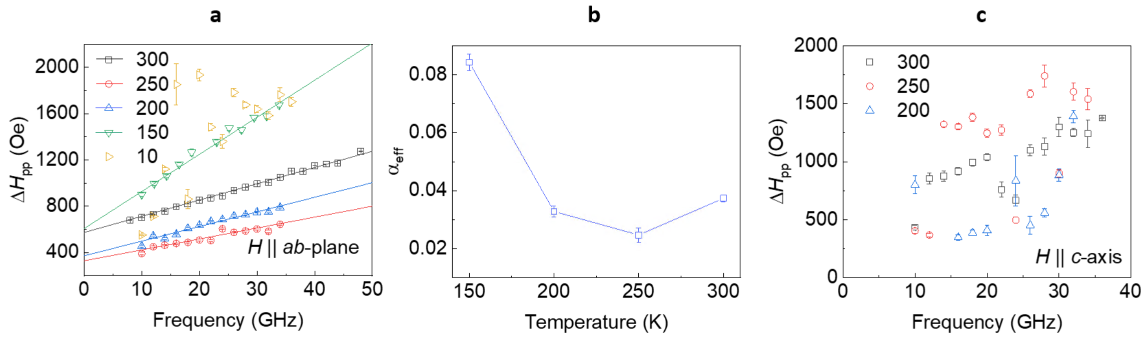

Figure 3.7: Characterization of FMR linewidth in Fe_5GeTe_2.[55] **a**. Peak-to-peak linewidth ΔH_{pp} vs. frequency for $H\|ab$. **b**. Temperature dependence of effective damping parameter α_{eff} for $H\|ab$. **c**. ΔH_{pp} vs. frequency for $H\|c$.

ξ, but to higher order no intraband terms occur[69]. Besides intrinsic damping, due to non-uniform magnetization states and defects in the sample, the linewidth can be broadened by extrinsic scattering mechanisms such as inhomogeneous line broadening ΔH_0 and two-magnon scattering ΔH_{TMS}. Thus, the FMR linewidth ΔH_{pp} can be expressed by the following form:[70]

$$\Delta H_{\mathrm{pp}} = \frac{2\alpha_{\mathrm{eff}}}{\sqrt{3}|\gamma|}\frac{f}{2\pi} + \Delta H_0 + \Delta H_{\mathrm{TMS}} \tag{3.3}$$

Figures 3.7a,c plot the FMR linewidth versus frequency for $H\|ab$ and $H\|c$ cases, respectively. The linewidths were measured with a magnitude between 400 Oe to 2000 Oe for both cases. As shown in Figure 3.7a, the FMR linewidth increases when the temperature reduces from 300 K to 150 K. The linewidth becomes higher and very scattered below 150 K. This indicates extrinsic contributions in Fe_5GeTe_2 at lower temperatures. A previous study showed that when FeRh transitions from ferromagnetic to antiferromagnetic, this causes a significant increase of the FMR linewidth[71]. Other studies have shown a significant increase of the linewidth in magnetite as it undergoes the Verwey transition[72], and of the effective damping in Py/Gd bilayers when approaching the Gd ordering temperature[66]. It is likely that the increased linewidth observed can also arise from similar magnetic phase transitions. In fact, Ref. [25] has proposed that Fe_5GeTe_2 transitions from ferromagnetic to ferrimagnetic at 275 K, and then transitions to a state with glassy clusters below 110 K. While the AC susceptibility results show no indication of a state with glassy clusters, the low-temperature FMR measurements support the argument of ferromagnetic to ferrimagnetic transitions at lower temperatures. Thus, Fe_5GeTe_2 has a very intriguing and complex magnetism and a complete understanding will require further studies.

The FMR measurements have shown that Fe_5GeTe_2 exhibits a similar damping constant to that of soft 3D magnets, when interpreting the slope of the linewidth as an effective Gilbert damping parameter. As can be seen from Figure 3.7b, the effective damping parameter α_{eff} ranges from 0.025 to 0.085 as temperature reduces from 300 K to 150 K. Table 3.1 provides a comparison of the Gilbert damping constant for typical materials. It can be seen that the reported vdW magnets have similar damping constants as 3D magnets. The α_{eff} of Fe_5GeTe_2 is similar to that of soft 3D transition metal magnets such as Permalloy.[73] Because the α_{eff} of Fe_5GeTe_2 is estimated from the $H\|ab$ measurements, it is likely that ΔH_{TMS} also contributes to α_{eff}.

Table 3.1: Summary of measured effective Gilbert damping constants for different materials at different temperatures.

Material	**type**	**Gilbert damping constant**	**Temperature**	**Source**
NiFe (permalloy) thin film (3 nm)	3D-conducting	0.013	300 K	Ref. [73]
$\mathbf{Fe_5GeTe_2}$	2D-conducting	0.035	300 K	This work
$\mathbf{Fe_5GeTe_2}$	2D-conducting	0.007	10 K	This work
$\mathbf{CrBr_3}$	2D-insulating	0.009	30 K	Ref. [74]
$\mathbf{Cr_2Ge_2Te_6}$	2D-insulating	0.01-0.08	10 K	Ref. [75]

3.5 DC and AC Susceptibility Measurements

DC and AC susceptibilities were measured to investigate if Fe_5GeTe_2 experiences glassiness at lower temperatures as reported in Ref.[25]. Figures 3.8a,b show the DC susceptibility measurements for the first thermal cycle after crystal growth and a subsequent thermal cycle, respectively. The cooling and heating were performed under a constant external field $H = 100$ Oe.

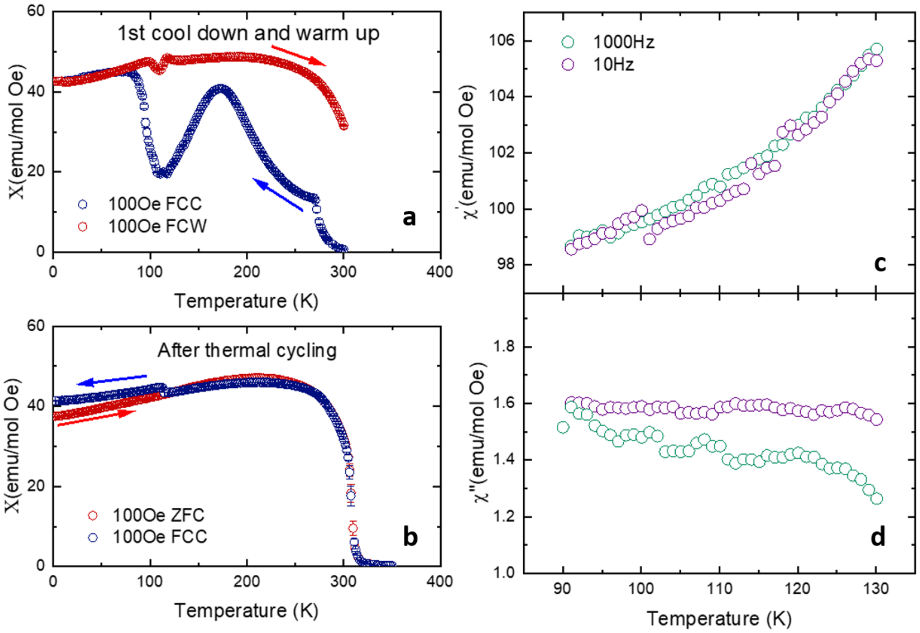

Figure 3.8: DC and AC susceptibilities in Fe_5GeTe_2.[55] **a** Field cooled DC susceptibility curves showing the first thermal cycle after crystal growth. **b** Field cooled DC susceptibility curves showing a subsequent thermal cycle. In both **a** and **b**, the DC susceptibility was measured while the sample was cooled (FCC) then warmed (FCW) with an external field = 100 Oe. **c** AC susceptibility plots showing the real part of the AC susceptibility. **d** AC susceptibility plots showing the imaginary part. The susceptibility was measured at two AC frequencies: 10 Hz (purple) and 1000 Hz (green).

Intriguingly, upon the first cool down, the DC susceptibility indicates a Curie temperature $T_c \sim 270$ K and a dramatic response around $T \sim 110$ K. The subsequent heating of the sample shows an enhanced T_c, indicating a possible transition to a metastable phase different from the one after initial crystal growth. Similar thermal cycling effects were reported in Ref.[21, 22]. Subsequent thermal cycles of DC susceptibility measurements show consistent behavior that is different from the initial cool down, as can be seen in Figure 3.8b. To investigate the intriguing behavior around $T \sim 110$ K, AC susceptibility was measured at different AC frequencies. According to Ref. [76], the transition to a glassy state usually manifests as a peak on the curve plotting the real part of the AC susceptibility χ' vs. temperature. The measurements do not show peaks of χ' around 110 K (Figure 3.84b), and appear to be not consistent with the glassy cluster state below 110 K as proposed in Ref.[25].

3.6 Measurements of Other Fe_5GeTe_2 Samples

During the growth process of Fe_5GeTe_2, bulk crystals from several batches were tested. The results demonstrated above are from a bulk crystal that showed experimental results most closely resembling what has already been reported in the literature. Here, we show measurements on a second bulk Fe_5GeTe_2 crystal that showed slightly different behaviors, but still exhibited similar key properties, e.g., anisotropic g-factor for $H\|ab$ and for $H\|c$ cases.

Figure 3.9 summarizes the relevant result from the VSM and FMR measurements of the second Fe_5GeTe_2 bulk crystal. Figure 3.9a shows the temperature dependent Magnetization versus field measurements for a field applied along the *ab*-plane (solid lines) and along the *c*-axis (dashed lines). These curves confirm that this Fe_5GeTe_2 crystal behaves similarly to the one discussed in the above sections. Specifically, both Fe_5GeTe_2 crystals have similar saturation field, saturation magnetization, coercivity, and anisotropy for all temperatures for both $H\|ab$ and $H\|c$ cases. Interestingly, the $H\|ab$ curves in Figure 3.9a differ from the curves in Figure 3.2a in that they are missing the additional slope change observed at temperatures 100 K and below. Such slope change was also reported in ref. [25].

Figure 3.9b confirms the Curie temperature of the second Fe_5GeTe_2 crystal through measurements of the field-cooled magnetization versus temperature curves for $H\|ab$ and for $H\|c$. For both cases, the Fe_5GeTe_2 crystal was cooled at a field $H =$ 50 Oe. The Curie temperature extracted from the curve is ∼332 K, similar to the one reported for the sample discussed in the sections above. The response of this second

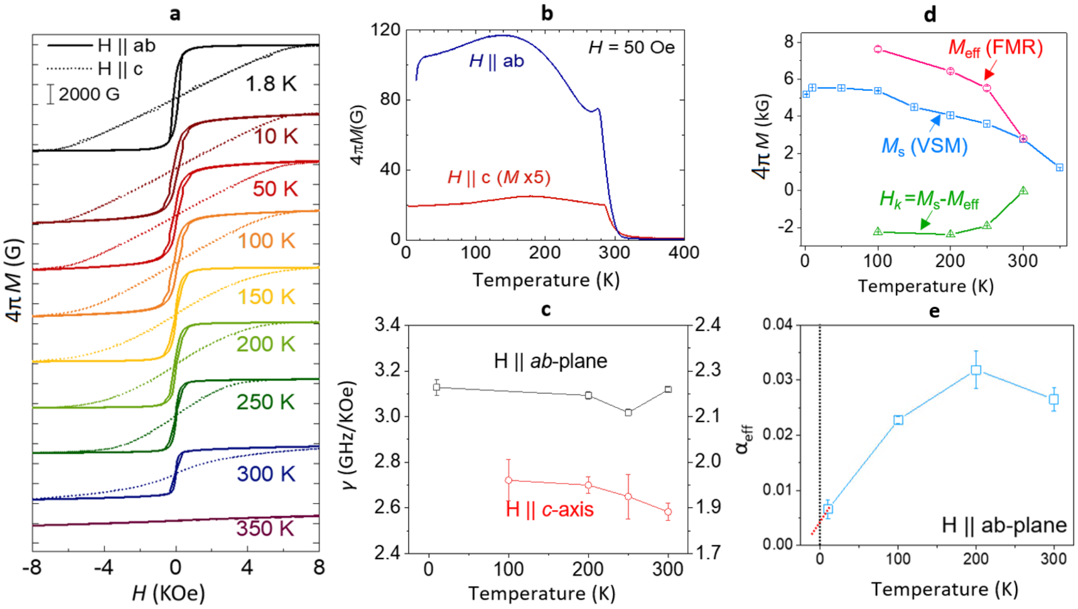

Figure 3.9: Measurements of a different Fe_5GeTe_2 bulk crystal.[55] **a** Temperature-dependent hysteresis loops for $H\|c$ (dashed lines) and $H\|ab$ (solid lines). **b** Field-cooled curves ($H = 50$ Oe) for the $H\|c$ (blue) and the $H\|ab$ (red) cases, respectively. **c** Temperature dependence of the gyromagnetic ratio γ and spectroscopic g-factor for the $H\|c$ (red) and $H\|ab$ (black) cases, respectively. **d** Temperature dependence of saturation magnetization $4\pi M_s$ and effective magnetization $4\pi M_{eff}$ from VSM and FMR measurements, respectively. **e** Temperature dependence of effective damping parameter α_{eff} for $H\|ab$.

Fe_5GeTe_2 crystal is missing the sharp drop between 200 K and 100 K, observed in Figure 3.2b.

FMR measurements were carried out for this sample in a similar fashion to the one performed on the first sample and discussed in the sections above. The resulting gyromagnetic ratio, g-factor, and effective magnetization from fitting the FMR data are shown in Figures 3.9c and 3.9d, respectively. The g-factor shows slightly different values but similar to the first sample, exhibits anisotropy depending on the direction of the external field. This again indicates orbital moment contribution to the magnetic moment in Fe_5GeTe_2. The effective magnetization values of this sample are higher than the saturation magnetization, indicating different crystalline anisotropy fields in the bulk crystal, as shown in Figure 3.9d.

The difference in magneto-crystalline anisotropy between the two samples may be attributed to subtle differences in the Fe content,[16] which can lead to different magneto-crystalline anisotropies, and subsequently the slightly different behavior observed in the VSM and FMR measurements.

Finally, the effective damping of this Fe_5GeTe_2 sample is plotted versus temperature in Figure 3.9e. The effective damping constant changes between 0.004 and 0.035 at different temperatures. The effective damping constant of this Fe_5GeTe_2 crystal reduces with reducing temperature, with an extrapolated value at 0 K $\sim$ 0.004, close to the value of the damping constant theoretically calculated for Fe_3GeTe_2 recently[64].

Thus, various quasi-static magnetization properties and magnetization dynamics in Fe_5GeTe_2 were explored. Part of the results in this chapter has been published in Ref. [55].

Chapter 4

Electronic Orbital Magnetism in a Quasi-Two-Dimensional Topological Magnon Insulator

4.1 Introduction

The previous chapter explored the magnetic properties of a room-temperature 2D vdWs magnet. This chapter focuses on a material that has a significantly lower Curie temperature, but nonetheless show very intriguing behavior due to the fact that it is a topological magnon insulator. Cu(1,3-bdc) crystal is used as a model material to study the correlation of Landé g-factor and orbital angular momentum through Vibrating Sample Magnetometry (VSM) and broadband Ferromagnetic Resonance (FMR) spectroscopy. The experimental results show an anisotropic gyromagnetic ratio and a corresponding g-factor tensor. This anisotropy is found to be correlated with the difference in IP and OOP saturation magnetization at lower temperatures ($T < 4$ K); it indicates the contribution of electronic orbital moment. Surprisingly, such correlation breaks down when $T > 4$ K.

Further analysis reveals that magnon-mediated electronic orbital moment has contributed to the magnetic moment at higher temperatures. The work presented in this chapter builds a foundation for uncovering the intriguing magnetization dynamics in Cu(1,3-bdc), and highlights the unique properties of this quasi-2D topological magnon insulator.

4.2 Quasi-Static Magnetization.

It was previously shown that, in the ground state of Cu(1,3-bdc), the spins within each Kagome plane are ferromagnetically ordered, while the spins in the neighboring planes are antiferromagnetically ordered. The interlayer antiferromagnetic coupling was found to be $\sim 0.3\%$ of the intralayer nearest-neighbor coupling. Thus, the magnetization across different Kagome planes can be easily aligned by a weak magnetic field ($\sim$ tens of mT)[29].

The quasi-static magnetization data of Cu(1,3-bdc) are presented in Figure 4.1. Here, several notes should be made: First, the magnetization as a function of IP and OOP fields at temperatures ranging from 1.9 K to 9 K was measured; consistent with previous measurements[29], the magnetization curves show that the easy axis of Cu(1,3-bdc) is IP (Figure 4.1b). Second, while the transition temperature of Cu(1,3-bdc) was reported to be $\sim$1.8 K[29], strong magnetization can be detected at temperatures up to 9 K. This is because Cu(1,3-bdc) is a quasi-2D material; significant short-range magnetic order arises in individual layers before 3D long-range order develops at a much lower temperature (i.e., 1.8 K). Thus, the magnetic transitions in Cu(1,3-bdc) can be summarized as follows: when T<1.8 K, Cu(1,3-bdc) exhibits long-range magnetic order. At temperatures higher but still close to the transition temperature, i.e. 1.8 K<T<$\sim$ 9 K, the long-range order gradually transitions to short-range order. At T>9 K, it transitions into a mostly paramagnetic state. Third, the magnetization curves were fitted with a hyperbolic tangent function[77] (Refer to Appendix A) to extract the saturation magnetization M_{s}. The temperature dependence of the IP and OOP saturation magnetization $M_{\mathrm{s,IP}}$, $M_{\mathrm{s,OOP}}$ is plotted in Figure 4.1c. Intriguingly, $M_{\mathrm{s,IP}}$ is higher than that of $M_{\mathrm{s,OOP}}$ across all tested temperatures. At 1.9 K, $M_{\mathrm{s,IP}}$ is 8.3% larger than $M_{\mathrm{s,OOP}}$, which is consistent with a separate magnetization measurement[29].

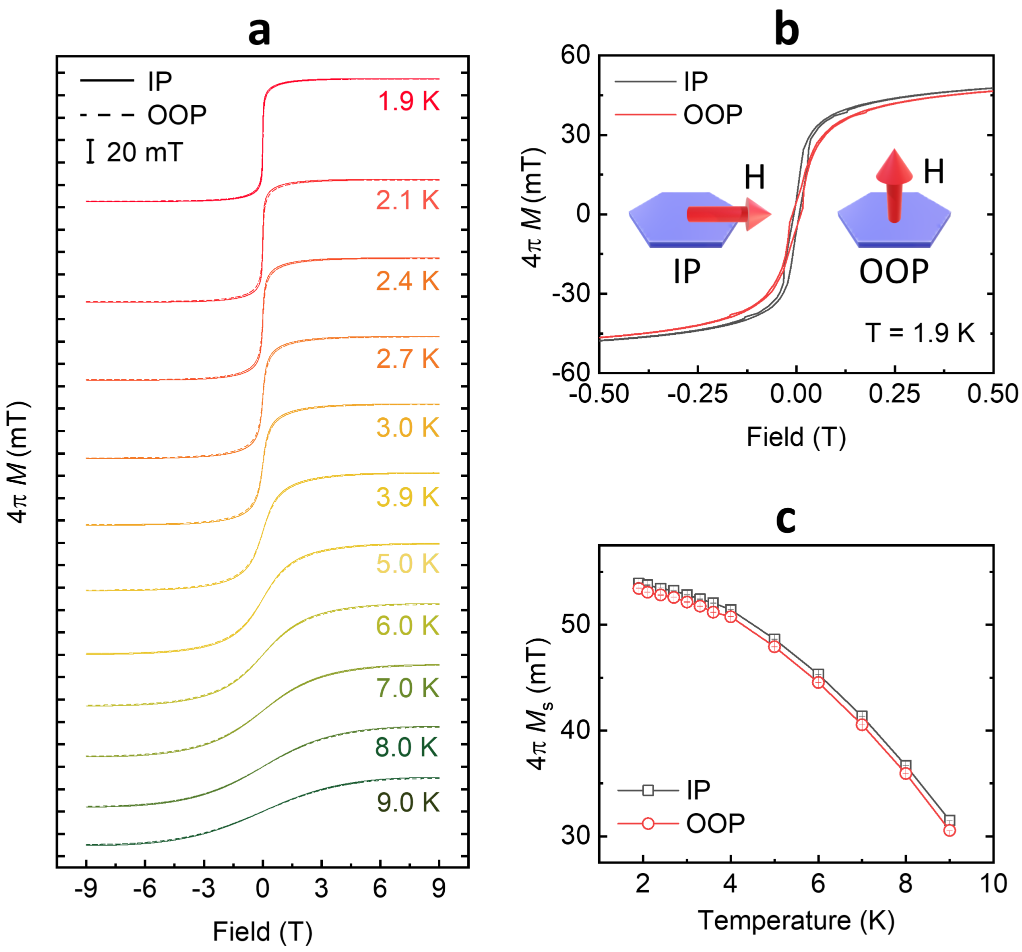

Figure 4.1: Quasi-static magnetic properties of Cu(1,3-bdc). **a.** Magnetization vs. externally applied field plots at different temperatures. The magnetic field was applied along the Kagome plane (IP) of the Cu(1,3-bdc) sample (solid lines), and perpendicular (OOP) to the Kagome plane (dashed lines). **b.** Zoomed-in IP and OOP hysteresis loops at T = 1.9 K, showing IP anisotropy. The left and right insets show the IP and OOP field directions, respectively. **c.** Temperature dependence of $M_{\mathrm{s,IP}}$ (gray) and $M_{\mathrm{s,OOP}}$(red) extracted from the VSM measurements.

To examine if the sample has uniaxial anisotropy in-plane, it was rotated and measured at different IP angles: 0°, 90°, and 120°. Figure 4.2 shows IP angular VSM measurements at 1.9 K, 5 K, and 9 K, respectively. At each temperature, the curves at different angles almost overlap with each other and no significant differences are observed. Therefore, it can be concluded that Cu(1,3-bdc) is an easy-plane magnet, and does not show uniaxial IP anisotropy.

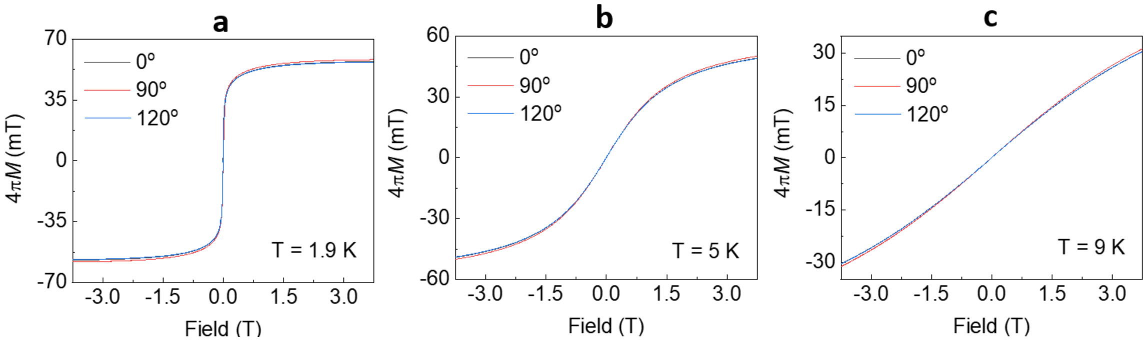

Figure 4.2: In-plane VSM measurements of Cu(1,3-bdc). **a.,b., and c.** VSM hysteresis loops at IP angles 0°, 90°, and 120° at 1.9 K, 5 K, and 9 K, respectively.

With the hypothesis that the difference in $M_{\mathrm{s,IP}}$ and $M_{\mathrm{s,OOP}}$ has resulted from orbital magnetic moment[50, 51], magnetization dynamics measurements to verify this understanding are carry out and discussed in the following section.

4.3 Magnetization Dynamics with FMR Spectroscopy.

Figure 4.3 presents the FMR data. A schematic of the FMR measurement is shown in Figure 4.3a. A microwave diode and lock-in amplifier were used for signal detection. A Vector Network Analyzer (VNA) was also used to perform the FMR measurements, and generated consistent data, as will be discussed further below. Figures 4.3b,c show the microwave power absorption vs. the external field at microwave frequencies ranging from 3 GHz to 27 GHz at 1.9 K along the IP and OOP directions, respectively. The FMR profiles were measured at temperatures up to 10 K. At each microwave frequency f, the FMR profiles were fitted to Lorentzian + anti-Lorentzian functions[56, 60] to extract the resonance field H_{r}, as well as the Full Width at Half Maximum (FWHM) linewidth ΔH_{FWHM}. The resonance frequencies are plotted against the fitted IP and OOP resonance fields as shown in Figures 4.3d,e. H_{r}-H_{offset} is adopted as the horizontal axes, where H_{r} is the resonance field, and H_{offset} = 0.4 T. Because H_{r} ($\geq$ 0.4 T) is about 9 times that of the magnetic anisotropy field

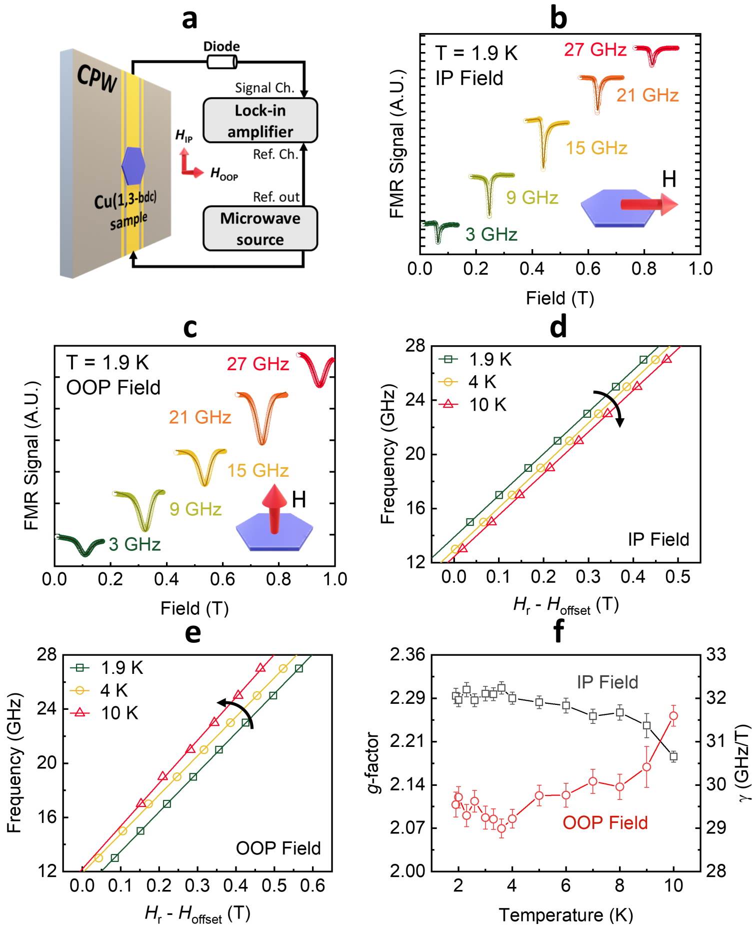

Figure 4.3: Broadband FMR spectroscopy and analysis. **a.** Schematic of the experimental setup. **b.** and **c.** FMR profiles measured at different microwave frequencies at T = 1.9 K for IP and OOP fields, respectively. Both the datapoints and fitted curves are presented. The insets in **b** and **c** show the IP and OOP field directions, respectively. **d.** and **e.** Kittel dispersion curves showing the resonance frequency f vs. resonance field H_r-H_offset at 1.9 K, 4 K, and 10 K for external fields applied IP and OOP, respectively. Here, H_offset = 0.4 T. The data points are fitted to Equations 1 and 2, respectively. The arrows show the behavior with increasing temperature. **f.** Temperature dependence of the Landé g-factor (left axis) and gyromagnetic ratio γ (right axis) for external fields along the IP (gray) and OOP (red) directions.

H_k ($\leq$ 0.05 T), the data points can be fitted to the revised Kittel equations when H_r $>>$ H_k (refer to Appendix C)[60]:

$$f = \gamma'_\mathrm{IP}(H_r + 2\pi H_\mathrm{eff}) \tag{4.1}$$

$$f = \gamma'_\mathrm{OOP}(H_r - 4\pi H_\mathrm{eff}) \tag{4.2}$$

Equations (4.1) and (4.2) are for the IP and OOP cases, respectively. Here, f is the microwave frequency, $\gamma' = \frac{\gamma}{2\pi}$ is the reduced gyromagnetic ratio, H_{r} is the resonance field, and H_{eff} is the effective field representing the contribution from magnetocrystalline anisotropy. The g-factor is calculated using $g = |\gamma|\frac{\hbar}{\mu_{\mathrm{B}}}$, where μ_{B} is the Bohr magneton and $\hbar$ is the reduced Planck constant.

Figure 4.3f plots the temperature dependence of the g-factor (left Y-axis) and γ' (right Y-axis) along the IP and OOP fields, respectively. Several observations can be made from Figure 4.3f: First, in both IP and OOP cases, the g-factor deviates from $g = 2$ that is for a free electron without orbital momentum. The deviation from $g = 2$ indicates an orbital contribution to the magnetic moment in Cu(1,3-bdc)[62, 55]. Second, g_{IP} is significantly larger than g_{OOP} at lower temperatures (i.e., <9 K). Third, the thermal evolution of g_{IP} and g_{OOP} shows opposite trends: g_{IP} reduces with increasing temperature, while g_{OOP} increases with increasing temperature.

Both the quasi-static and dynamic magnetization measurements indicate the contribution of orbital moment. Thus, the difference in the g-factor $\Delta g = g_{\mathrm{IP}}$-$g_{\mathrm{OOP}}$ is compared with the difference of the saturation magnetization $\Delta M_{\mathrm{s}} = M_{\mathrm{s,IP}}$-$M_{\mathrm{s,OOP}}$, as shown in Figure 4.7a. Figure 4.7a shows two contrasting behaviors, a low-temperature regime where the behavior of Δg is closely correlated with ΔM_{s} at T <4 K, and a high-temperature regime where Δg deviates greatly from ΔM_{s} at T >4 K.

4.3.1 VNA Measurements

To confirm the results above, the FMR measurements were performed using a VNA. Figures 4.4a-d (e-h) show the measured VNA response at different frequencies and external IP (OOP) magnetic field. In these plots, the color represents the S12 signal magnitude. Figure 4.5 presents the extracted resonance frequency as a function of the resonance fields. The data points are fitted to Eq. (4.1) and (4.2).

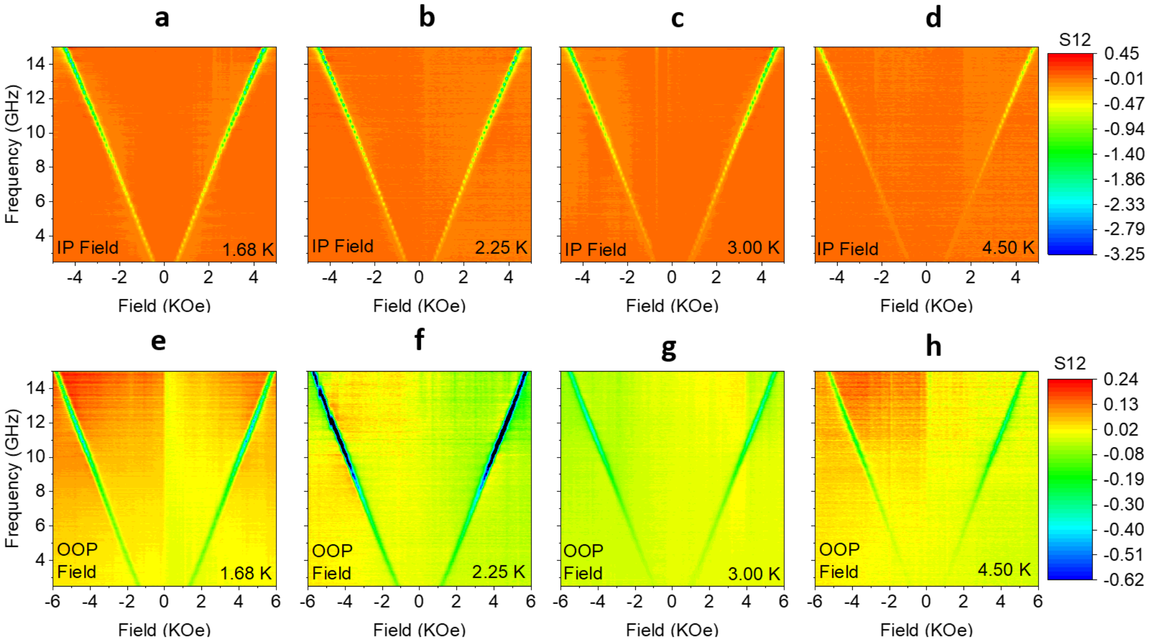

Figure 4.4: VNA FMR measurements of Cu(1,3-bdc) at different temperatures. **a.-d.** Frequency vs. IP field at 1.68 K, 2.25 K, 3.00 K, and 4.5 K, respectively. **e.-f.** Frequency vs. OOP field at 1.68 K, 2.25 K, 3.00 K, and 4.5 K, respectively. For all plots, the color represents the amplitude of the S12 signal.

The gyromagnetic ratio and corresponding g-factor values, obtained from fitting the VNA data, show excellent agreement with the results acquired from the microwave diode-based measurement, as shown in Figure 4.6a. In the figure, "Diode" refers to the diode-based FMR measurements, where a microwave diode was used to detect the microwave absorption. As can be seen from Figure 4.6a, the VNA and diode methods have yielded very similar g-factor and gyromagnetic ratio γ values. Figure 4.6b plots temperature dependence of Δg and ΔM_{s}. The results further show that the VNA and diode methods exhibit good agreement, where they both deviate from ΔM_{s} at higher temperatures.

It is insightful to interpret the temperature-dependent anisotropy of the g-factor in terms of the dynamics of orbital magnetism. At low temperatures, the g-factor anisotropy can be attributed to the anisotropy of the orbital magnetization in Cu(1,3-bdc) along the IP and OOP directions, with the IP case having a larger orbital

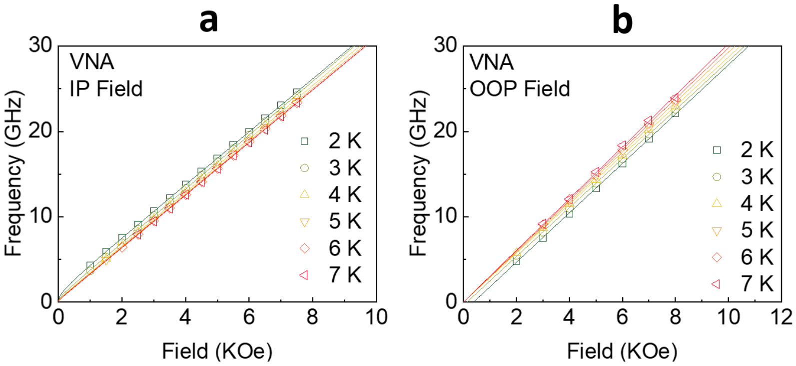

Figure 4.5: Kittel dispersion curves from the VNA measurements. **a.** The Frequency f vs. resonance field H_r at 2 K, 3 K, 4 K, 5 K, 6 K, and 7 K for an externally applied IP field. The data points are fitted to Eq. (2). **b.** Frequency f vs. resonance field H_r at 2 K, 3 K, 4 K, 5 K, 6 K, and 7 K for an externally applied OOP field. The data points are fitted to Eq. (3).

contribution. The deviation of Δg from ΔM_s at higher temperatures comes as a surprise, because they are expected to be closely correlated at all temperatures. Thus, this points to a different mechanism to the orbital correction of the g-factor; it cannot be explained by the orbital motion of the electrons around atomic cores.

4.4 Electronic Topological Orbital Moment

A recent theoretical work uncovered contributions to electronic orbital magnetism originating from spin chirality generated from spin disorder[42, 78]. This new development in the area of thermally-driven spin fluctuations points out a route to explain the observed behavior in Cu(1,3-bdc). According to the theory, the non-vanishing net spin chirality can arise even in a collinear fluctuating spin system in its ground state. This can be directly translated into a topological electronic orbital motion, of which the strength is given by the topological orbital susceptibility relating the degree of the chirality to the magnitude of the orbital magnetization [79]. The magnitude of the topological orbital susceptibility can be sizable in materials with weak spin-orbit coupling, i.e. Cu(1,3-bdc), as shown in conventional microscopic calculations. Furthermore, in ferromagnetic Kagome systems with non-trivial topological magnonic

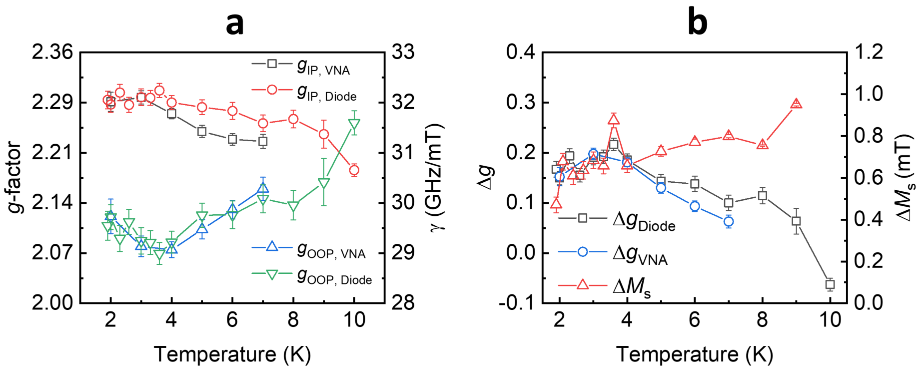

Figure 4.6: Comparison of VNA and microwave diode-based FMR data. **a.** Temperature dependence of the IP and OOP g-factor and gyromagnetic ratio γ from both the VNA and microwave diode measurements. **b.** Correlation between VNA and microwave diode Δg (plotted on the left axis), and $\Delta\ M_{\mathrm{s}}$ (plotted on the right axis), as a function of temperature.

bands, the spin chirality mediated by thermal fluctuations has been shown to imprint sizeable electronic orbital magnetization; their sign and magnitude can be controlled by the parameters of the studied system [42].

Following the approach in Ref. [42], the extracted parameters which describe the spin exchange interactions in Cu(1,3-bdc) [48] are used to compute the magnonic properties. The calculation has yielded thermally induced net chirality and the corresponding orbital magnetization in the system. Specifically, the effective spin Hamiltonian of Cu(1,3-bdc) is used in Eq.(4.3):

$$\begin{aligned} H = &-\frac{1}{2}\sum_{ij} J_{ij}\mathbf{S}_i\cdot\mathbf{S}_j - \frac{1}{2}\sum_{ij}\mathbf{D}_{ij}\cdot(\mathbf{S}_i\times\mathbf{S}_j) \\ &- \mathbf{B}\cdot\kappa^{\mathrm{TO}}\sum_{ijk}\hat{\mathbf{e}}_{ijk}[\hat{\mathbf{S}}_i\cdot(\hat{\mathbf{S}}_j\times\hat{\mathbf{S}}_k)] - \mu_{\mathrm{B}}g_e\mathbf{B}\cdot\sum_i\mathbf{S}_i\,, \end{aligned} \tag{4.3}$$

where J_{ij} mediates the Heisenberg exchange between spins $\mathbf{S}_{\mathrm{i}}$ and $\mathbf{S}_{\mathrm{j}}$ on sites i and j in the first term. The second term is the antisymmetric Dzyaloshinskii-Moriya Interaction (DMI) quantified by vectors $\mathbf{D}_{\mathrm{ij}}$. The fourth term couples the spins to an external magnetic field $\mathbf{B}$. The third term is the ring-exchange interaction term, which explicitly describes the Zeeman interaction of the topological orbital moment (TOM, $\mathbf{L}^{\mathrm{TOM}}$) with the external magnetic field $\mathbf{B}$ [42]. TOM marks a special type of electronic orbital moment. This term is given by the product of the scalar spin chirality (SSC) and the topological orbital susceptibility κ^{TO} [78, 80, 79, 81]. Owing to the symmetry of the planar Kagome lattice, both the TOM and the DMI vectors are perpendicular to the Kagome plane (OOP), in the same direction as the applied external magnetic field $\mathbf{B}$. In Eq.(4.3), the spin operator $\mathbf{S}_{\mathrm{i}}$ at site i is set as $\frac{1}{2}$, g_{e} is set as 2, the nearest-neighbor exchange interaction J is chosen as 0.6 meV and the DMI vector is set as $D_{\mathrm{ij}} = (0, 0, 0.09)$ meV. The topological orbital susceptibility κ^{TO} is chosen as a typical value of $-0.2\mu_{\mathrm{B}}$, motivated by the previous material studies [78, 80, 79, 81].

Figure 4.7b plots the magnonic band-resolved contributions to the orbital moment in Cu(1,3-bdc) for $B = 0$. At low energies, between the first and second modes, one can observe a strong correlation between the orbital moment and the topological band inversion of magnonic bands. The contribution of the band-resolved orbital moment is integrated to the overall orbital moment of Cu(1,3-bdc) at finite temperatures. Figure 4.7c presents the calculated TOM as a function of temperature and polar angle θ that indicates the magnetization direction. From Figure 4.7c, two observations are made: first, the analysis shows that the symmetry of the system allows orbital magnetization originating from spin excitations in the OOP case, but not the IP case. Second, the value of the thermally-induced orbital moment increases monotonously with temperature; it can reach sizeable values at T >4 K. The results suggest that the g-factor should increase with temperature for an OOP field, but decrease for an IP field due to thermal fluctuations. Thus, our theory accurately predicts the general trend and the change in the sign of Δg observed experimentally, as shown in Figure 4.7d. This suggests that the spin excitations can renormalize the fundamental quantum mechanical constant conventionally associated with the atomic

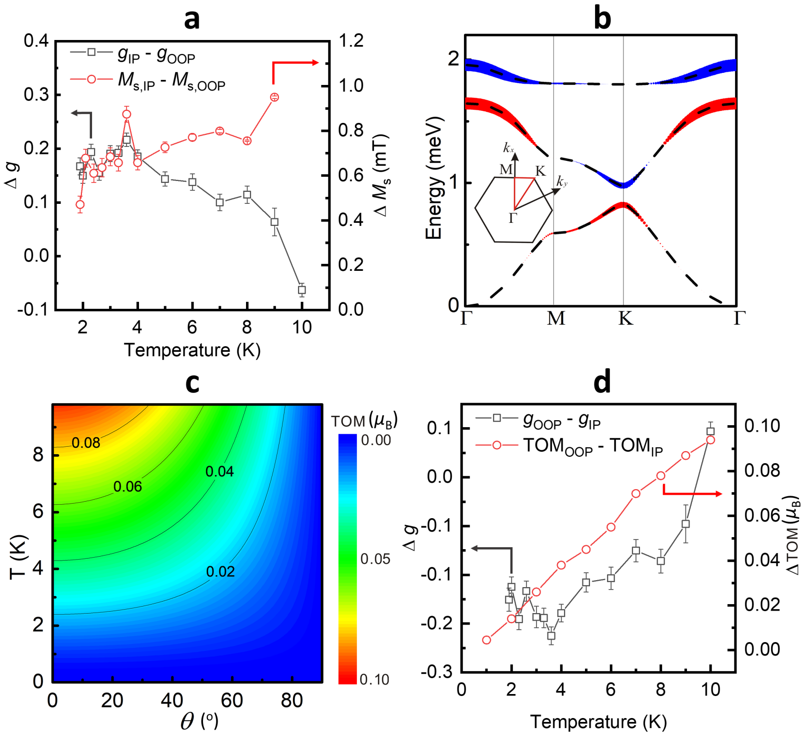

Figure 4.7: **a.** Temperature dependence of Δg (plotted on the left Y-axis) and $\Delta M_{\rm s}$ (plotted on the right Y-axis). **b.** Flat band analysis for the magnonic bands of Cu(1,3-bdc). Red and blue colors represent the positive and negative signs of the local topological orbital moment (TOM) $\mathbf{L}^{\rm TOM}$, respectively. The line thickness denotes the corresponding magnitude. The insert represents the first Brillouin Zone. The red lines connect the high symmetry points which are selected in the dispersion. **c.** TOM magnitude vs. temperature and polar angle θ. θ=0^o (90^o) means that magnetization is along the OOP (IP) direction. The colors represent the magnitude of the integrated TOM in $\mu_{\rm B}$. B is assumed to be zero. **d.** Δg (left Y-axis) and ΔTOM (right Y-axis) as a function of temperature.

orbital magnetism. In this regard, these finding has brought up a new mechanism for orbital dynamics in topological magnonic systems.

Figure 4.8 summarizes the different orbital contributions to the magnetic moment discussed above. At low temperatures, for both IP and OOP cases, the orbital contributions come from the motions of electrons orbiting their atomic cores. The black arrows in the left two illustrations represent the summation of the spin and the orbital angular momentum of the orbiting electron (red) around the nucleus (yellow). When the temperature increases, as shown in the right illustration, the thermal

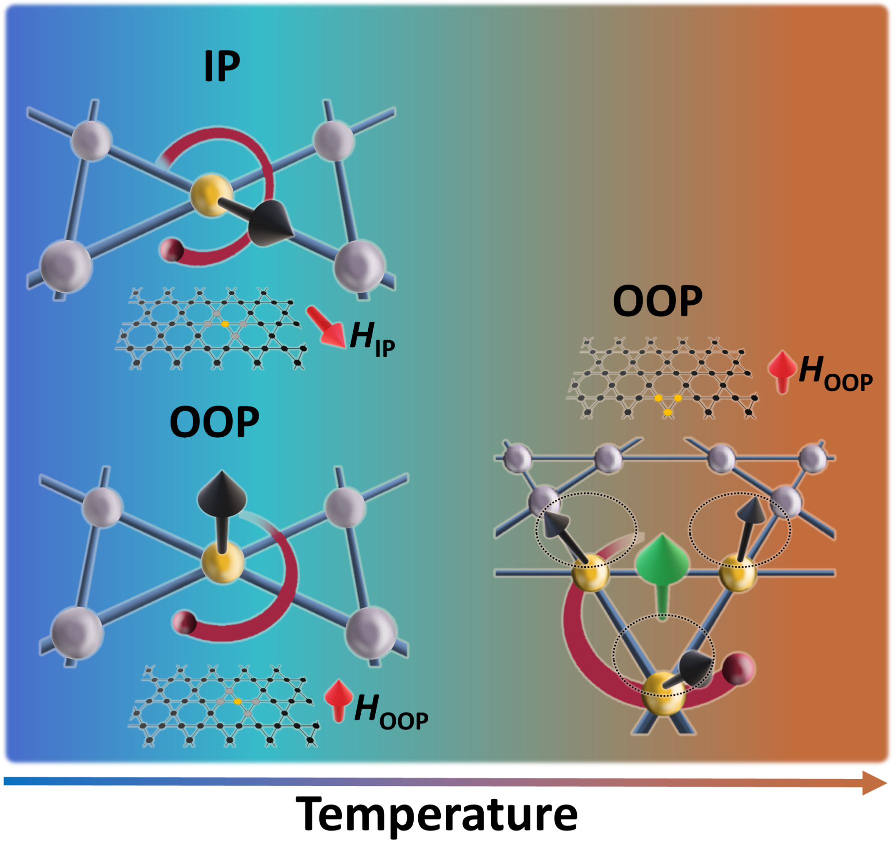

Figure 4.8: Orbital contributions to the magnetic moment. The left two illustrations show the electronic orbital moment occurring at low temperatures. The black arrows represent the overall spin and orbital moment for a field applied IP (top left) and OOP (bottom left). The bottom right illustration shows the magnon-mediated topological orbital moment (green arrow) arising from thermally-driven scalar spin chirality.

fluctuations give rise to spin chirality allowed by the symmetry of the Kagome lattice in the OOP case. An electron (red), hopping between a precessing noncolinear spin-triplet (yellow), generates topological orbital moment (green arrow). This TOM leads to the increase of the OOP g-factor with increasing temperature.

4.5 FMR Linewidth Analysis

The FMR fittings discussed above also generate the Full-width-at-half-maximum (FWHM) linewidth ΔH_{FWHM}. ΔH_{FWHM} is plotted as a function of temperature at different microwave frequencies, as shown in Figure 4.9. ΔH_{FWHM} remains almost

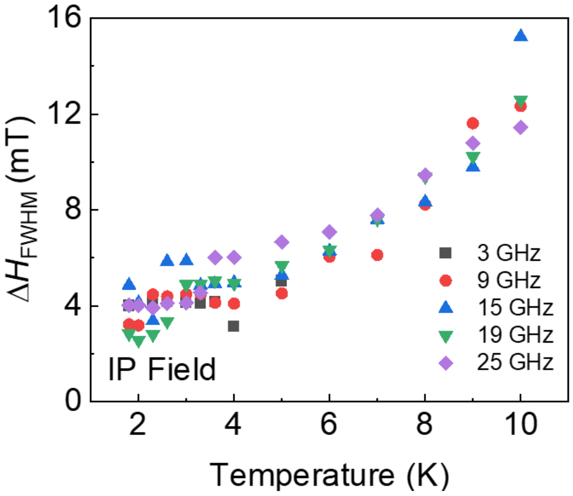

Figure 4.9: Full-width-at-half-maximum (FWHM) linewidth ΔH_{FWHM} vs. temperature at different microwave frequencies for IP field.

constant up to T $\sim$ 3 K, which is close to T_c of Cu(1,3-bdc). As the temperature increases past 3 K, ΔH_{FWHM} starts to increase monotonically. The linewidth vs. temperature can be understood as follows: at lower temperature (T <4 K), Cu(1,3-bdc) becomes more ferromagnetic (long-range magnetic ordering), and the spin arrangement becomes more uniform. In addition, the magnon-phonon scattering at reduced temperature is lower. These two mechanisms lead to lower linewidths at lower temperatures. At higher temperatures (T >4 K), the short-range magnetic ordering, and increased magnon-phonon scattering contribute to the broadened linewidths.

Chapter 5

Summary and Future Work

The research works can be summarized as two parts. For Fe_5GeTe_2, single crystals have been synthesized and show a bulk Curie temperature of 332 K. While the Curie temperature of Fe_5GeTe_2 is expected to decrease when the vdWs crystal is exfoliated into thin layers[27], the bulk value is still one of the highest recorded for a vdWs bulk magnet until now, making it an attractive 2D option to be used in spintronic devices. Both VSM and FMR were employed to study the magnetic properties of the Fe_5GeTe_2 samples. The experiments were performed with external magnetic fields applied along the *c*-axis and the *ab*-plane directions from 300 K to 10 K. The temperature and field dependences of the *g*-factor and spin scattering mechanisms were explored. The *g*-factor along the *ab*-plane was found to be larger than that along the *c*-axis, indicative of considerable orbital momentum arising from spin-orbit coupling in Fe_5GeTe_2. The FMR analysis also revealed low temperature-enhanced linewidth broadening, together with the VSM data, they indicate a ferromagnetic to ferrimagnetic transition at lower T. For future studies, it will be interesting to exploit Fe_5GeTe_2 thin films for spin transport and spin-to-charge conversion experiments at room temperature. In addtion, Fe_5GeTe_2 opens new ways to build and study hybrid magnonic structures.

For Cu(1,3-bdc), anisotropies of Landé *g*-factor and saturation magnetization were observed in Cu(1,3-bdc) along the ab- and c-axes of the Kagome plane. When T <4 K, the differences of *g*-factor (Δg) and saturation magnetization (ΔM_{s}) were found to be closely correlated, which indicates contribution of orbital moment of electrons to the magnetic moment. The deviation of Δg and ΔM_{s} at T >4 K can be explained by the spin chirality mediated by thermal fluctuations inducing sizeable electronic orbital magnetization. Our work has highlighted Cu(1,3-bdc) as an important platform to understand the interplay of topology, spin excitations and orbital magnetism, thereby presenting potential direction for establishing new material platforms for building novel spintronic devices. Moreover, this work has pointed out a new way to probe the orbital moment in quantum magnets via the g-factor measurements. Future work that studies the chiral and topological orbital magnetism of domain walls and skyrmions[82], as well as skyrmion-topological magnon interactions in Cu(1,3-bdc) is of great interest[36].

In the future, the groundwork laid out in this thesis could be expanded upon as follows:

- The Fe_5GeTe_2 single crystals can be exfoliated into thin layers and studied for understanding the evolution of the magnetic properties, including Curie temperature, saturation magnetization, magnetic anisotropy, and thermal evolution of the g-factor.
- Thin, or monolayers, of Fe_5GeTe_2 single crystals can be fabricated into Hall bars and studied with electrotransport measurements to understand the spin dynamics using optical ferromagnetic resonance[83].
- Field-assisted magnetic force microscopy (MFM) and electrotransport can be used to investigate the possibility of nucleating and transporting skyrmions in few-layer Fe_5GeTe_2, and to study domain walls and domain wall motion.
- Hall bars fabricated on Cu(1,3-bdc) samples can be used to perform voltage-gating experiments using ionic liquid to investigate the possibility of raising its Curie temperature and altering its magnetic properties.
- Specially designed FMR setup, along with ionic liquid gating, can be used to alter the magnetization dynamics in Cu(1,3-bdc), which can then be studied for

possible spin-transport enhancements and interplay of topology and dynamic magnetization.

Bibliography

[1] R. L. Stamps, S. Breitkreutz, J. Åkerman, A. V. Chumak, Y. Otani, G. E. W. Bauer, J.-U. Thiele, M. Bowen, S. A. Majetich, M. Kläui, I. L. Prejbeanu, B. Dieny, N. M. Dempsey, and B. Hillebrands, "The 2014 magnetism roadmap," *Journal of Physics D: Applied Physics*, vol. 47, p. 333001, jul 2014.

[2] S. Chikazumi, *Physics of Magnetism.* John Wiley and Sons, Ltd., 1984.

[3] S. Blundell, "Magnetism in condensed matter," 2003.

[4] K. S. Burch, D. Mandrus, and J.-G. Park, "Magnetism in two-dimensional van der waals materials," *Nature*, vol. 563, pp. 47–52, Nov 2018.

[5] S. Geller and M. Gilleo, "The crystal structure and ferrimagnetism of yttrium-iron garnet, $y_3fe_2(feo_4)_3$," *Journal of Physics and Chemistry of Solids*, vol. 3, no. 1, pp. 30 – 36, 1957.

[6] R. Frisenda, Y. Niu, P. Gant, M. Muñoz, and A. Castellanos-Gomez, "Naturally occurring van der waals materials," *npj 2D Materials and Applications*, vol. 4, p. 38, Oct 2020.

[7] K. F. Mak, J. Shan, and D. C. Ralph, "Probing and controlling magnetic states in 2d layered magnetic materials," *Nature Reviews Physics*, vol. 1, pp. 646–661, Nov 2019.

[8] S. B. Mitta, M. S. Choi, A. Nipane, F. Ali, C. Kim, J. T. Teherani, J. Hone, and W. J. Yoo, "Electrical characterization of 2d materials-based field-effect transistors," *2D Materials*, vol. 8, no. 1, p. 012002, 2020.

[9] L. D. Casto, A. J. Clune, M. O. Yokosuk, J. L. Musfeldt, T. J. Williams, H. L. Zhuang, M.-W. Lin, K. Xiao, R. G. Hennig, B. C. Sales, J.-Q. Yan, and D. Mandrus, "Strong spin-lattice coupling in crsite3," *APL Materials*, vol. 3, no. 4, p. 041515, 2015.

[10] V. Carteaux, D. Brunet, G. Ouvrard, and G. Andre, "Crystallographic, magnetic and electronic structures of a new layered ferromagnetic compound cr2ge2te6," *Journal of Physics: Condensed Matter*, vol. 7, pp. 69–87, jan 1995.

[11] I. Tsubokawa, "On the magnetic properties of a crbr3 single crystal," *Journal of the Physical Society of Japan*, vol. 15, no. 9, pp. 1664–1668, 1960.

[12] M. A. McGuire, H. Dixit, V. R. Cooper, and B. C. Sales, "Coupling of crystal structure and magnetism in the layered, ferromagnetic insulator cri3," *Chemistry of Materials*, vol. 27, no. 2, pp. 612–620, 2015.

[13] H.-J. Deiseroth, K. Aleksandrov, C. Reiner, L. Kienle, and R. K. Kremer, "Fe3gete2 and ni3gete2 – two new layered transition-metal compounds: Crystal structures, hrtem investigations, and magnetic and electrical properties," *European Journal of Inorganic Chemistry*, vol. 2006, no. 8, pp. 1561–1567, 2006.

[14] B. Chen, J. Yang, H. Wang, M. Imai, H. Ohta, C. Michioka, K. Yoshimura, and M. Fang, "Magnetic properties of layered itinerant electron ferromagnet fe3gete2," *Journal of the Physical Society of Japan*, vol. 82, no. 12, p. 124711, 2013.

[15] M. Bander and D. L. Mills, "Ferromagnetism of ultrathin films," *Phys. Rev. B*, vol. 38, pp. 12015–12018, Dec 1988.

[16] J. Seo, D. Y. Kim, E. S. An, K. Kim, G.-Y. Kim, S.-Y. Hwang, D. W. Kim, B. G. Jang, H. Kim, G. Eom, S. Y. Seo, R. Stania, M. Muntwiler, J. Lee, K. Watanabe,

T. Taniguchi, Y. J. Jo, J. Lee, B. I. Min, M. H. Jo, H. W. Yeom, S.-Y. Choi, J. H. Shim, and J. S. Kim, “Nearly room temperature ferromagnetism in a magnetic metal-rich van der waals metal,” *Science Advances*, vol. 6, no. 3, 2020.

[17] Y. Deng, Y. Yu, Y. Song, J. Zhang, N. Z. Wang, Z. Sun, Y. Yi, Y. Z. Wu, S. Wu, J. Zhu, J. Wang, X. H. Chen, and Y. Zhang, “Gate-tunable room-temperature ferromagnetism in two-dimensional fe3gete2,” *Nature*, vol. 563, pp. 94–99, Nov 2018.

[18] Z. Li, W. Xia, H. Su, Z. Yu, Y. Fu, L. Chen, X. Wang, N. Yu, Z. Zou, and Y. Guo, “Magnetic critical behavior of the van der waals fe5gete2 crystal with near room temperature ferromagnetism,” *Scientific Reports*, vol. 10, p. 15345, Sep 2020.

[19] J.-X. Zhu, M. Janoschek, D. S. Chaves, J. C. Cezar, T. Durakiewicz, F. Ronning, Y. Sassa, M. Mansson, B. L. Scott, N. Wakeham, E. D. Bauer, and J. D. Thompson, “Electronic correlation and magnetism in the ferromagnetic metal $\mathrm{fe}_3\mathrm{gete}_2$,” *Phys. Rev. B*, vol. 93, p. 144404, Apr 2016.

[20] V. Y. Verchenko, A. A. Tsirlin, A. V. Sobolev, I. A. Presniakov, and A. V. Shevelkov, “Ferromagnetic order, strong magnetocrystalline anisotropy, and magnetocaloric effect in the layered telluride fe3-δgete2,” *Inorganic Chemistry*, vol. 54, no. 17, pp. 8598–8607, 2015. PMID: 26267350.

[21] A. F. May, D. Ovchinnikov, Q. Zheng, R. Hermann, S. Calder, B. Huang, Z. Fei, Y. Liu, X. Xu, and M. A. McGuire, “Ferromagnetism near room temperature in the cleavable van der waals crystal fe5gete2,” *ACS Nano*, vol. 13, no. 4, pp. 4436–4442, 2019. PMID: 30865426.

[22] A. F. May, C. A. Bridges, and M. A. McGuire, "Physical properties and thermal stability of $\mathrm{fe}_{5-x}\mathrm{gete}_2$ single crystals," *Phys. Rev. Materials*, vol. 3, p. 104401, Oct 2019.

[23] Z. Fei, B. Huang, P. Malinowski, W. Wang, T. Song, J. Sanchez, W. Yao, D. Xiao, X. Zhu, A. F. May, W. Wu, D. H. Cobden, J.-H. Chu, and X. Xu, "Two-dimensional itinerant ferromagnetism in atomically thin fe3gete2," *Nature Materials*, vol. 17, pp. 778–782, Sep 2018.

[24] J. Stahl, E. Shlaen, and D. Johrendt, "The van der waals ferromagnets fe5–δgete2 and fe5–δ–xnixgete2 – crystal structure, stacking faults, and magnetic properties," *Zeitschrift für anorganische und allgemeine Chemie*, vol. 644, no. 24, pp. 1923–1929, 2018.

[25] H. Zhang, R. Chen, K. Zhai, X. Chen, L. Caretta, X. Huang, R. V. Chopdekar, J. Cao, J. Sun, J. Yao, R. Birgeneau, and R. Ramesh, "Itinerant ferromagnetism in van der waals $\mathrm{fe}_{5-x}\mathrm{gete}_2$ crystals above room temperature," *Phys. Rev. B*, vol. 102, p. 064417, Aug 2020.

[26] Y. Gao, Q. Yin, Q. Wang, Z. Li, J. Cai, T. Zhao, H. Lei, S. Wang, Y. Zhang, and B. Shen, "Spontaneous (anti)meron chains in the domain walls of van der waals ferromagnetic fe5-xgete2," *Advanced Materials*, vol. 32, no. 48, p. 2005228, 2020.

[27] T. Ohta, K. Sakai, H. Taniguchi, B. Driesen, Y. Okada, K. Kobayashi, and Y. Niimi, "Enhancement of coercive field in atomically-thin quenched fe5gete2," *Applied Physics Express*, vol. 13, p. 043005, mar 2020.

[28] K. Yamagami, Y. Fujisawa, B. Driesen, C. H. Hsu, K. Kawaguchi, H. Tanaka, T. Kondo, Y. Zhang, H. Wadati, K. Araki, T. Takeda, Y. Takeda, T. Muro, F. C. Chuang, Y. Niimi, K. Kuroda, M. Kobayashi, and Y. Okada, "Itinerant

ferromagnetism mediated by giant spin polarization of the metallic ligand band in the van der waals magnet fe_5Gete_2," *Phys. Rev. B*, vol. 103, p. L060403, Feb 2021.

[29] R. Chisnell, J. S. Helton, D. E. Freedman, D. K. Singh, F. Demmel, C. Stock, D. G. Nocera, and Y. S. Lee, "Magnetic transitions in the topological magnon insulator cu(1,3-bdc)," *Phys. Rev. B*, vol. 93, p. 214403, Jun 2016.

[30] M. Z. Hasan and C. L. Kane, "Colloquium: Topological insulators," *Rev. Mod. Phys.*, vol. 82, pp. 3045–3067, Nov 2010.

[31] F. Haldane and S. Raghu, "Possible realization of directional optical waveguides in photonic crystals with broken time-reversal symmetry," *Physical review letters*, vol. 100, no. 1, p. 013904, 2008.

[32] S. Raghu and F. D. M. Haldane, "Analogs of quantum-hall-effect edge states in photonic crystals," *Physical Review A*, vol. 78, no. 3, p. 033834, 2008.

[33] F. Li, X. Huang, J. Lu, J. Ma, and Z. Liu, "Weyl points and fermi arcs in a chiral phononic crystal," *Nat. Phys.*, vol. 14, no. 1, p. 30, 2018.

[34] L. Zhang, J. Ren, J.-S. Wang, and B. Li, "Topological magnon insulator in insulating ferromagnet," *Phys. Rev. B*, vol. 87, p. 144101, Apr 2013.

[35] M. Malki and G. S. Uhrig, "Topological magnetic excitations," *EPL (Europhysics Letters)*, vol. 132, p. 20003, oct 2020.

[36] M. Pereiro, D. Yudin, J. Chico, C. Etz, O. Eriksson, and A. Bergman, "Topological excitations in a kagome magnet," *Nature Communications*, vol. 5, p. 4815, Sep 2014.

[37] M. Malki and G. S. Uhrig, "Topological magnon bands for magnonics," *Phys. Rev. B*, vol. 99, p. 174412, May 2019.

[38] H. Kondo, Y. Akagi, and H. Katsura, “Three-dimensional topological magnon systems,” *Phys. Rev. B*, vol. 100, p. 144401, Oct 2019.

[39] A. Mook, S. A. Díaz, J. Klinovaja, and D. Loss, “Chiral hinge magnons in second-order topological magnon insulators,” *arXiv preprint arXiv:2010.04142*, 2020.

[40] A. A. Kovalev and V. Zyuzin, “Spin torque and nernst effects in dzyaloshinskii-moriya ferromagnets,” *Phys. Rev. B*, vol. 93, no. 16, p. 161106, 2016.

[41] R. Cheng, S. Okamoto, and D. Xiao, “Spin nernst effect of magnons in collinear antiferromagnets,” *Phys. Rev. Lett.*, vol. 117, no. 21, p. 217202, 2016.

[42] L.-c. Zhang, D. Go, J.-P. Hanke, P. M. Buhl, S. Grytsiuk, S. Blügel, F. R. Lux, and Y. Mokrousov, “Imprinting and driving electronic orbital magnetism using magnons,” *Commun. Phys.*, vol. 3, no. 1, pp. 1–8, 2020.

[43] L. Zhang, J. Ren, J.-S. Wang, and B. Li, “Topological nature of the phonon hall effect,” *Physical review letters*, vol. 105, no. 22, p. 225901, 2010.

[44] P. Li, W. Wu, Y. Wen, C. Zhang, J. Zhang, S. Zhang, Z. Yu, S. A. Yang, A. Manchon, and X.-x. Zhang, “Spin-momentum locking and spin-orbit torques in magnetic nano-heterojunctions composed of weyl semimetal wte2,” *Nature Communications*, vol. 9, p. 3990, Sep 2018.

[45] R. A. Niyazov, D. N. Aristov, and V. Y. Kachorovskii, “Coherent spin transport through helical edge states of topological insulator,” *npj Computational Materials*, vol. 6, p. 174, Nov 2020.

[46] Y. Araki, T. Misawa, and K. Nomura, “Long-range spin transport on the surface of topological dirac semimetal,” *Phys. Rev. Research*, vol. 3, p. 023219, Jun 2021.

[47] E. A. Nytko, J. S. Helton, P. Müller, and D. G. Nocera, “A structurally perfect s = 1/2 metal-organic hybrid kagomé antiferromagnet,” *Journal of the American Chemical Society*, vol. 130, pp. 2922–2923, Mar 2008.

[48] R. Chisnell, J. S. Helton, D. E. Freedman, D. K. Singh, R. I. Bewley, D. G. Nocera, and Y. S. Lee, “Topological magnon bands in a kagome lattice ferromagnet,” *Phys. Rev. Lett.*, vol. 115, p. 147201, Sep 2015.

[49] D. Malz, J. Knolle, and A. Nunnenkamp, “Topological magnon amplification,” *Nature Communications*, vol. 10, p. 3937, Sep 2019.

[50] H. Chen, T.-C. Wang, D. Xiao, G.-Y. Guo, Q. Niu, and A. H. MacDonald, “Manipulating anomalous hall antiferromagnets with magnetic fields,” *Phys. Rev. B*, vol. 101, p. 104418, Mar 2020.

[51] R. R. Neumann, A. Mook, J. Henk, and I. Mertig, “Orbital magnetic moment of magnons,” *Phys. Rev. Lett.*, vol. 125, p. 117209, Sep 2020.

[52] K. Fabian, V. P. Shcherbakov, and S. A. McEnroe, “Measuring the curie temperature,” *Geochemistry, Geophysics, Geosystems*, vol. 14, no. 4, pp. 947–961, 2013.

[53] M. Hansen and S. Mørup, “Estimation of blocking temperatures from zfc/fc curves,” *Journal of Magnetism and Magnetic Materials*, vol. 203, no. 1, pp. 214 – 216, 1999.

[54] R. Cheng, M. Li, A. Sapkota, A. Rai, A. Pokhrel, T. Mewes, C. Mewes, D. Xiao, M. De Graef, and V. Sokalski, “Magnetic domain wall skyrmions,” *Phys. Rev. B*, vol. 99, p. 184412, May 2019.

[55] L. Alahmed, B. Nepal, J. Macy, W. Zheng, B. Casas, A. Sapkota, N. Jones, A. R. Mazza, M. Brahlek, W. Jin, M. Mahjouri-Samani, S. S.-L. Zhang, C. Mewes,

L. Balicas, T. Mewes, and P. Li, “Magnetism and spin dynamics in room-temperature van der waals magnet fe5gete2,” *2D Materials*, vol. 8, p. 045030, sep 2021.

[56] C. Oates, F. Ogrin, S. Lee, P. Riedi, G. Smith, and T. Thomson, “High field ferromagnetic resonance measurements of the anisotropy field of longitudinal recording thin-film media,” *Journal of Applied Physics*, vol. 91, pp. 1417–1422, 02 2002.

[57] V. Flovik, F. Macià, A. D. Kent, and E. Wahlström, “Eddy current interactions in a ferromagnet-normal metal bilayer structure, and its impact on ferromagnetic resonance lineshapes,” *Journal of Applied Physics*, vol. 117, no. 14, p. 143902, 2015.

[58] M. Harder, Z. X. Cao, Y. S. Gui, X. L. Fan, and C.-M. Hu, “Analysis of the line shape of electrically detected ferromagnetic resonance,” *Phys. Rev. B*, vol. 84, p. 054423, Aug 2011.

[59] N. Mecking, Y. S. Gui, and C.-M. Hu, “Microwave photovoltage and photoresistance effects in ferromagnetic microstrips,” *Phys. Rev. B*, vol. 76, p. 224430, Dec 2007.

[60] H. Chang, P. Li, W. Zhang, T. Liu, A. Hoffmann, L. Deng, and M. Wu, “Nanometer-thick yttrium iron garnet films with extremely low damping,” *IEEE Magnetics Letters*, vol. 5, pp. 1–4, 2014.

[61] A. Rai, A. Sapkota, A. Pokhrel, M. Li, M. De Graef, C. Mewes, V. Sokalski, and T. Mewes, “Higher-order perpendicular magnetic anisotropy and interfacial damping of co/ni multilayers,” *Phys. Rev. B*, vol. 102, p. 174421, Nov 2020.

[62] S. Khan, C. W. Zollitsch, D. M. Arroo, H. Cheng, I. Verzhbitskiy, A. Sud, Y. P. Feng, G. Eda, and H. Kurebayashi, "Spin dynamics study in layered van der waals single-crystal $\mathrm{cr}_2\mathrm{ge}_2\mathrm{te}_6$," *Phys. Rev. B*, vol. 100, p. 134437, Oct 2019.

[63] K. Kim, J. Seo, E. Lee, K.-T. Ko, B. S. Kim, B. G. Jang, J. M. Ok, J. Lee, Y. J. Jo, W. Kang, J. H. Shim, C. Kim, H. W. Yeom, B. Il Min, B.-J. Yang, and J. S. Kim, "Large anomalous hall current induced by topological nodal lines in a ferromagnetic van der waals semimetal," *Nature Materials*, vol. 17, pp. 794–799, Sep 2018.

[64] M. Costa, N. M. R. Peres, J. Fernández-Rossier, and A. T. Costa, "Nonreciprocal magnons in a two-dimensional crystal with out-of-plane magnetization," *Phys. Rev. B*, vol. 102, p. 014450, Jul 2020.

[65] P. Bruno, "Tight-binding approach to the orbital magnetic moment and magnetocrystalline anisotropy of transition-metal monolayers," *Phys. Rev. B*, vol. 39, pp. 865–868, Jan 1989.

[66] B. Khodadadi, J. B. Mohammadi, C. Mewes, T. Mewes, M. Manno, C. Leighton, and C. W. Miller, "Enhanced spin pumping near a magnetic ordering transition," *Phys. Rev. B*, vol. 96, p. 054436, Aug 2017.

[67] V. Kamberský, "Spin-orbital gilbert damping in common magnetic metals," *Phys. Rev. B*, vol. 76, p. 134416, Oct 2007.

[68] D. M. Edwards, "The absence of intraband scattering in a consistent theory of gilbert damping in pure metallic ferromagnets," *Journal of Physics: Condensed Matter*, vol. 28, p. 086004, feb 2016.

[69] A. T. Costa and R. B. Muniz, "Breakdown of the adiabatic approach for magnetization damping in metallic ferromagnets," *Phys. Rev. B*, vol. 92, p. 014419, Jul 2015.

[70] S. Jiang, L. Sun, Y. Yin, Y. Fu, C. Luo, Y. Zhai, and H. Zhai, "Ferromagnetic resonance linewidth and two-magnon scattering in fe1-xgdx thin films," *AIP Advances*, vol. 7, no. 5, p. 056029, 2017.

[71] Y. Wang, M. M. Decker, T. N. G. Meier, X. Chen, C. Song, T. Grünbaum, W. Zhao, J. Zhang, L. Chen, and C. H. Back, "Spin pumping during the antiferromagnetic–ferromagnetic phase transition of iron–rhodium," *Nature Communications*, vol. 11, p. 275, Jan 2020.

[72] A. Srivastava, A. V. Singh, J. B. Mohammadi, C. Mewes, A. Gupta, and T. Mewes, "Ferromagnetic resonance study of the verwey phase transition of magnetite thin film on mgga$_2$o$_4$(001) substrate," *IEEE Transactions on Magnetics*, vol. 56, no. 12, pp. 1–6, 2020.

[73] Y. Zhao, Q. Song, S.-H. Yang, T. Su, W. Yuan, S. S. P. Parkin, J. Shi, and W. Han, "Experimental investigation of temperature-dependent gilbert damping in permalloy thin films," *Scientific Reports*, vol. 6, p. 22890, Mar 2016.

[74] X. Shen, H. Chen, Y. Li, H. Xia, F. Zeng, J. Xu, H. Y. Kwon, Y. Ji, C. Won, W. Zhang, and Y. Wu, "Multi-domain ferromagnetic resonance in magnetic van der waals crystals cri3 and crbr3," *Journal of Magnetism and Magnetic Materials*, vol. 528, p. 167772, 2021.

[75] T. Zhang, Y. Chen, Y. Li, Z. Guo, Z. Wang, Z. Han, W. He, and J. Zhang, "Laser-induced magnetization dynamics in a van der waals ferromagnetic cr2ge2te6 nanoflake," *Applied Physics Letters*, vol. 116, no. 22, p. 223103, 2020.

[76] V. Cannella and J. A. Mydosh, "Magnetic ordering in gold-iron alloys," *Phys. Rev. B*, vol. 6, pp. 4220–4237, Dec 1972.

[77] P. Li, J. Ding, S. S.-L. Zhang, J. Kally, T. Pillsbury, O. G. Heinonen, G. Rimal, C. Bi, A. DeMann, S. B. Field, W. Wang, J. Tang, J. S. Jiang, A. Hoffmann,

N. Samarth, and M. Wu, “Topological hall effect in a topological insulator interfaced with a magnetic insulator,” *Nano Letters*, vol. 21, pp. 84–90, Jan 2021.

[78] S. Wimmer, S. Mankovsky, and H. Ebert, “Chirality-induced linear response properties in non-coplanar mn$_3$ge,” *Phys. Rev. B*, vol. 103, no. 2, p. 024437, 2021.

[79] S. Grytsiuk, J.-P. Hanke, M. Hoffmann, J. Bouaziz, O. Gomonay, G. Bihlmayer, S. Lounis, Y. Mokrousov, and S. Blügel, “Topological–chiral magnetic interactions driven by emergent orbital magnetism,” *Nat. Commun.*, vol. 11, no. 1, pp. 1–7, 2020.

[80] J.-P. Hanke, F. Freimuth, S. Blügel, and Y. Mokrousov, “Prototypical topological orbital ferromagnet γ-FeMn,” *Sci. Rep.*, vol. 7, p. 41078, 2017.

[81] J.-P. Hanke, F. Freimuth, A. K. Nandy, H. Zhang, S. Blügel, and Y. Mokrousov, “Role of berry phase theory for describing orbital magnetism: From magnetic heterostructures to topological orbital ferromagnets,” *Phys. Rev. B*, vol. 94, no. 12, p. 121114, 2016.

[82] F. R. Lux, F. Freimuth, S. Blügel, and Y. Mokrousov, “Engineering chiral and topological orbital magnetism of domain walls and skyrmions,” *Commun. Phys.*, vol. 1, no. 1, p. 60, 2018.

[83] Y. Xiong, Y. Li, R. Bidthanapally, J. Sklenar, M. Hammami, S. Hall, X. Zhang, P. Li, J. E. Pearson, T. Sebastian, G. Srinivasan, A. Hoffmann, H. Qu, V. Novosad, and W. Zhang, “Detecting phase-resolved magnetization dynamics by magneto-optic effects at 1550-nm wavelength,” *IEEE Transactions on Magnetics*, pp. 1–1, 2020.

Appendices

Appendix A

VSM data Fitting Procedure

For an accurate extraction of the saturation magnetization M_s values, the data collected from VSM measurements can be fitted to hyperbolic tangent functions as follows[1,2]

$$M(H) = M_\mathrm{s1} tanh(\frac{H \pm H_\mathrm{c1}}{H_{01}}) + M_\mathrm{s2} tanh(\frac{H \pm H_\mathrm{c2}}{H_{02}}) \tag{A.1}$$

Where H is the applied magnetic field, M_s1 and M_s2 are the saturation magnetization, H_c1 and H_c2 are the coercivity, and H_{01} and H_{02} are constants. One tangent function can be used to fit curves measured for purely ferromagnetic materials. However, for materials that have ferromagnetic individual layers, with interlayer antiferromagnetic coupling, such as in Cu(1,3-bdc), two tangent functions can used to account for the antiferromagnetically coupled spins. Figure A.1 shows an example of such fitting; the VSM data collected for Cu(1,3-bdc) at T = 1.9 K for an externally swept OOP field (red open circles) is fitted to Eq. (A.1) (solid black line).

---

[1] P. Li, J. Ding, S. S.-L. Zhang, J. Kally, T. Pillsbury, O. G. Heinonen, G. Rimal, C. Bi, A. DeMann, S. B. Field, W. Wang, J. Tang, J. S. Jiang, A. Hoffmann, N. Samarth, and M. Wu, "Topological hall effect in a topological insulator interfaced with a magnetic insulator," *Nano Letters*, vol. 21, pp. 84-90, Jan 2021.

[2] K. M. Fijalkowski, M. Hartl, M. Winnerlein, P. Mandal, S. Schreyeck, K. Brunner, C. Gould, and L. W. Molenkamp, "Coexistence of surface and bulk ferromagnetism mimics skyrmion hall effect in a topological insulator,"*Phys. Rev.X*, vol. 10, p. 011012, Jan 2020.

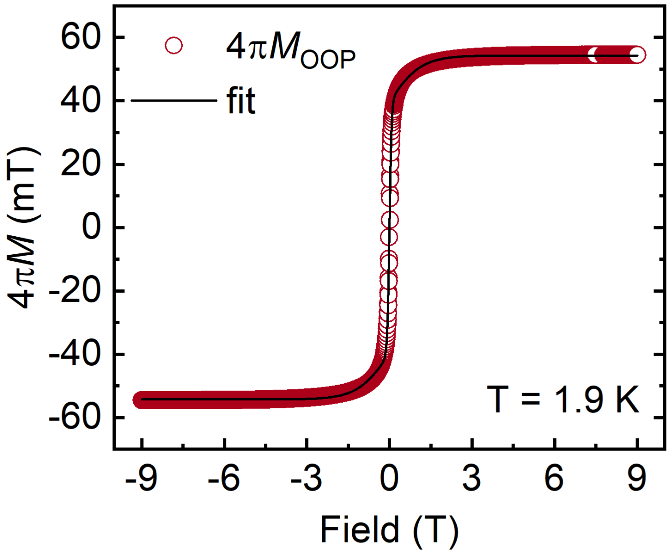

Figure A.1: Fitted Cu(1,3-bdc) VSM measurement for an OOP field at T = 1.9 K. The circular data points represent the raw measured VSM data. The solid black line shows the fit to Eq. A.1.

Appendix B

Broadband FMR Spectroscopy

B.1 Introduction to FMR

When an electron is subjected to an external field that does not align with its spin axis, as demonstrated in Figure B.1a, the electron starts to *precess* around the direction of the external field. The precession motion is governed by the Landau–Lifshitz equation[1,2]:

$$\frac{d\mathbf{M}}{dt} = -\gamma \mathbf{M} \times \mathbf{H}_{eff} - \alpha \frac{\gamma}{M_s} \mathbf{M} \times (\mathbf{M} \times \mathbf{H}_{eff}) \tag{B.1}$$

Where M is the magnetic moment of the electron, H_{eff} is the effective field, including the external applied field, as well as the demagnetization field, γ is the gyromagnetic ratio, which is the ratio of the electron's magnetic moment to its angular momentum (in units of GHz/KOe), M_{s} is the saturation magnetization, and α is the magnetic damping constant. The $M \times H_{\mathrm{eff}}$ term describes the field-like torque (FLT) pushing the electron to precess, while the $M \times M \times H_{\mathrm{eff}}$ term describes the damping like torque (DLT), pushing the electron to stop precessing and align its spin to the external field.

The precession frequency and direction is field and material dependent. If an external microwave field with a frequency matching that of the precession frequency of the electron (the resonance frequency) is applied, the electron is able to absorb the microwave power and its precession angle is maximized. This is equivalent to an

---

[1] A. Amikam,*Introduction to the Theory of Ferromagnetism.* Clarendon Press.,1996.

[2] T. Gilbert, "A lagrangian formulation of the gyromagnetic equation of the magnetization field,"*Phys. Rev.,* vol. 100, p. 1243, 1955.

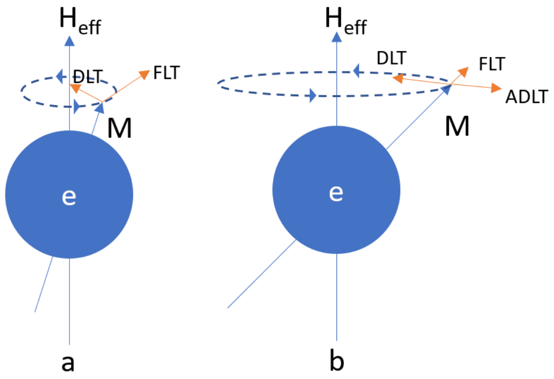

Figure B.1: Precession of an electron **a**: Under the influence of an external magnetic field, and **b**: under the influence of an external magnetic field and a resonant microwave field.

additional torque exerted on the electron spin, known as the anti-damping torque, which acts in the opposite direction of the damping torque, as demonstrated in Figure B.1b. In general, the stronger the external field is, the higher the microwave frequency needed for resonance.

The phenomenon occurring when a microwave field of a certain frequency is applied to a magnetic material, in the presence of an external field, such that its electrons collectively and homogeneously precess at a maximized angle, is referred to as *Ferromagnetic Resonance*, or FMR for short. The bases of FMR spectroscopy revolves around monitoring the microwave power loss at a certain frequency as an external magnetic field is swept. The process is repeated for several microwave frequencies, and the collected data is used to extract magnetic properties[3,4].

---

[3] E. Montoya, T. McKinnon, A. Zamani, E. Girt, and B. Heinrich, “Broadband fer-romagnetic resonance system and methods for ultra thin magnetic films,” *Journal of Magnetism and Magnetic Materials*, vol. 356, pp. 12 – 20, 2014.

[4] I. S. Maksymov and M. Kostylev, “Broadband stripline ferromagnetic resonance spectroscopy of ferromagnetic films, multilayers and nanostructures,” *Physica E: Low-dimensional Systems and Nanostructures*, vol. 69, pp. 253 – 293, 2015.

B.2 FMR System Configuration

There are two main methods to obtain FMR data: by monitoring the microwave power loss 1) while an external magnetic field is swept at a fixed microwave frequency, or 2) while the microwave frequency is swept at a fixed external magnetic Field. Thus, in order to perform broadband FMR spectroscopy, one would need a controllable magnetic field, a microwave field with controllable power and frequency, some form of waveguide to allow the microwaves to interact with the sample, and in cases where the samples have lower than room temperature Curie temperatures, a cooler to control the sample temperature. The DynaCool PPMS is capable of providing both the required external magnetic field, as well as temperature control that can cool a sample down to 1.6 K. For the microwave signal, one could use either a dedicated microwave source, and detect the signal separately, or use a device such as a vector network analyzer (VNA) to both generate and detect the microwave signal.

Separate detection of the direct microwave signal generated from a dedicated microwave source, and more importantly its power loss, with good signal-to-noise ratio, is challenging due to the high frequency nature of the signal. Therefore, modulation techniques are usually used to add an envelope to the signal with a much lower frequency (usually tens to hundreds of Hz), the lower frequency envelope can then be detected by a lock-in amplifier, and the power loss of the signal can be accurately monitored and recorded. The amplitude modulation is either configured in the microwave source itself, and the microwave's oscillator output is used as a reference, or it can be added through field modulation using Helmholtz coils. Co-planar waveguides (CPWs) are usually used in FMR experiments, as they can efficiently support a wide range of microwave frequencies[5]. The detected FMR signal also depends on the direction of the external field with respect to the sample (either IP or OOP), therefore for systems where the direction of the field cannot be controlled (such as the DynaCool

---

[5] R. Simons, *Coplanar Waveguide Circuits, Components, and Systems.* Wiley-IEEE, 2001.

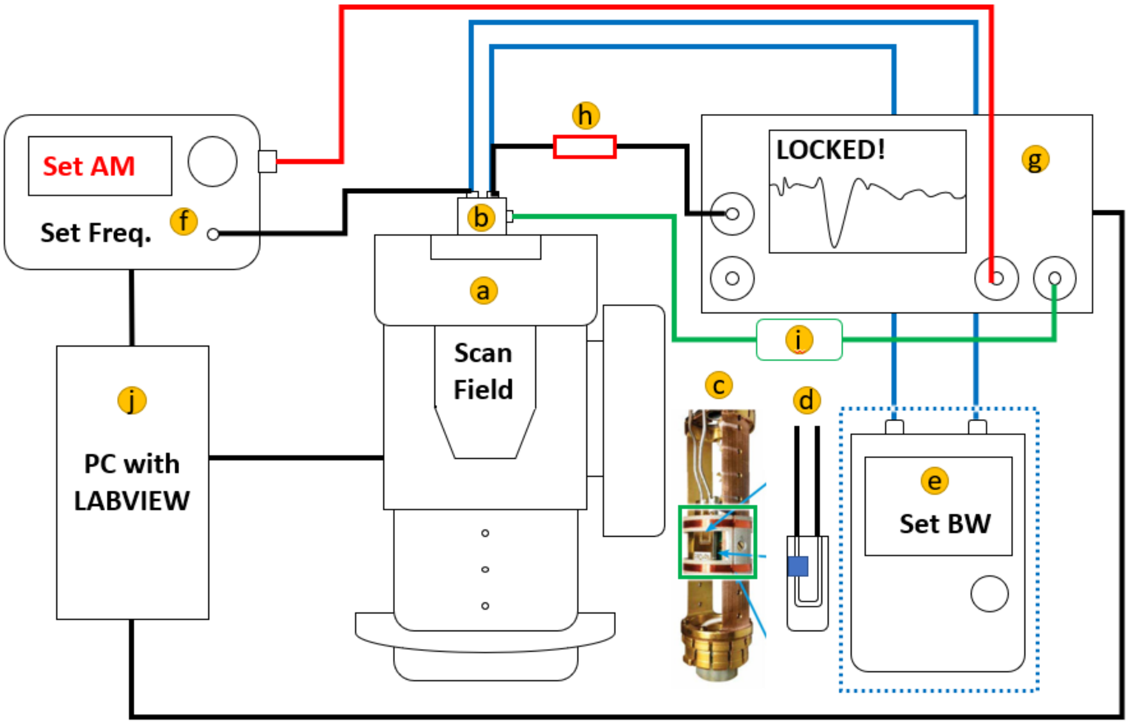

Figure B.2: Various FMR experimental setups using the DynaCool PPMS. More details in the text. **a.** Dynacool PPMS, **b.** FMR probe, **c.** FMR probe CPW holder, showing Helmholtz coils. **d.** Illustration of a CPW with a square sample. **e.** A portable VNA with two microwave ports. **f.** A microwave source. **g.** A lock-in amplifier. **h.** A microwave diode. **i.** A current amplifier. **j.** a PC to control the different equipment. Blue highlights represent equipment and connections present only when using a VNA. Red highlights represent equipment and connections present only when using amplitude modulation. Green highlights represent equipment and connections present only when using field modulation.

PPMS), the CPWs themselves come in two different configurations to allow for both IP and OOP measurements. Figure B.2 shows the various experimental setups that can be used. For all setups, a DynaCool PPMS with an equipped FMR probe is used. The FMR probe has two microwave ports for input/output, a CPW holder, a set of Helmholtz coils for field modulation, and a port to connect a source to the Helmholtz coils.

B.3 FMR Spectroscopy Using a VNA

Vector network analyzers come in different forms, even portable ones, such as the FieldFox F9918A, and they usually have two microwave ports, S1 and S2, that are both capable of sending and receiving microwave signals. In a VNA, one could measure the reflected signal of either ports: S11 or S22, or a signal could be sent from one port and detected from another: S12 or S21. For FMR spectroscopy, S12 or S21 are usually used: The microwave signal is sent from port S1 (S2), through the CPW with the sample under test, and into the port S2 (S1), where the power loss can be detected. FMR measurements with a VNA are usually performed by fixing an external magnetic field to a certain value, and then capturing the VNA S12 or S21 output across a broadband frequency range of interest. The measurement is repeated for different external magnetic field values.

Figure B.2 shows an FMR experimental setup. A sample is attached on top of the stripline of a CPW (usually by simply taping it to the CPW with kapton tape) as shown in B.2d, and then the CPW is attached to the CPW holder (B.2c) of the FMR probe, and its ends are connected to the FMR probe ports. Then, the FMR probe is inserted (B.2b) into the DynaCool PPMS (B.2a). A PC (B.2j) with special software, such as LabView, is used to control the magnetic field and temperature settings of the DynaCool PPMS. Next, the two VNA (B.2e) ports are connected to the two ports on the FMR probe (blue lines in Figure B.2). The VNA is then set to measure S12 or S21, and the frequency bandwidth of interest is set. The FieldFox F9918A has a bandwidth that spans the range from a few KHz, up to ~27GHz. For external magnetic fields $\leq$ 1 Tesla, for most ferromagnets, FMR can be detected within the frequency range: 2 GHz $\leq$ F $\leq$ 20 GHz (the higher the field, the higher the frequency needed for FMR is). Thus, a VNA is an ideal device to measure FMR in most cases.

After the experimental setup is complete, the following steps are performed to capture FMR data: 1) The frequency bandwidth of interest is set in the VNA. 2)

With the external field set to zero, the S12 (or S21) signal is saved. Since VNAs are highly sensitive, and due to background noise, a strong background signal can still be detected even at zero-field. This step measures this background noise so it can be subtracted from measurements performed when a field is applied. 3) A small magnetic field is applied (i. e. 250 Oe). 4) The S12 signal is saved. 5) The field is increased in steps, and each time step 3 is repeated. 6) If the measurements were performed using an IP CPW, steps 2-5 are repeated but with the OOP CPW setup instead. 7) If the FMR response at various temperatures is needed (such as to extract the Curie temperature), then steps 2-6 are repeated at different temperatures. 8) The data is processed by subtracting the zero-field signal (measured at a certain temperature and CPW) is subtracted from all field-dependent measurements. The data is then plotted and fitted.

B.4 FMR Spectroscopy Using a Diode and Lock-In Amplifier

If a dedicated microwave source is to be used instead of a VNA, then a lock-in amplifier can be used to detect the signal. This is possible by adding a low-frequency envelope to the microwave signal either from the source itself, or by using Helhmoltz coils to apply a small modulation field to the signal. A lock-in amplifier is used to greatly enhance the signal-to-noise ratio. By providing the lock-in with a reference signal with a fixed frequency, it locks in to that frequency, and only detects the signal that matches that frequency, filtering out any background noise with different frequencies. The reference signal can either be external (such as from the microwave source OSC out port, if amplitude modulation is used from the source itself), or it could be internal, by locking to the lock-in internal oscillator, and using the OSC out port on the lock-in to feed the modulation signal to the Helmholtz coils. The procedure for the two processes is broken down below.

Using the same DynaCool with FMR probe, CPW, and sample setup discussed at the beginning of the VNA section above, the FMR experiment with a dedicated microwave source is performed as follows: A microwave source with built-in amplitude modulation (Figure B.2f) is used. The microwave output is connected to one of the two FMR probe ports. The other FMR probe port is then connected to channel A input on a lock-in amplifier (B.2g), through a microwave diode (B.2h). The microwave diode produces a voltage signal proportional to the RF signal input, and helps in detecting the signal. Next, the OSC out port from the microwave source is connected to REF IN port in the lock-in (red line in Figure B.2). In addition to controlling the DynaCool field and temperature, a PC can be used to interface with the microwave source and lock-in to control them and read their outputs. While the VNA method measures the broadband frequency response at fixed magnetic fields, the lock-in method is performed with an opposite technique, where the microwave frequency is fixed, while the external field is scanned and the lock-in signal is recorded.

The full details to measure FMR after the above experimental setup is completed are as follows: 1) The microwave source is configured: The modulation depth (typically 15-30%) and frequency (typically 90-2000 Hz) are set. The power level (between -20 dBm and 20 dBm) must also be set, and the correct value is sample-dependent. Some samples show the best FMR signal at lower power levels, while others require high power levels to show appreciable signal. 2) The first microwave frequency of interest is set in the microwave source (typically 2 GHz). 3) The lock-in is set to external reference mode, and locks into the same modulation frequency set in the microwave source. 4) The lock-in response is recorded while the field is swept. The field is usually swept from a certain value to zero, not the other way around. If the approximate field signal at which FMR occurs is not known before hand, then a field that is large enough is chosen, then swept (usually at a rate of $\sim$25 Oe/sec) to zero. If the approximate FMR field is known or can be guessed beforehand, then the field sweep can be set up to start and stop at a margin slightly above and below the guessed value, in the interest of saving time. 5) The microwave source frequency is increased in steps (usually in steps of 1 GHz or 2 GHz) and at each step, step 4 is repeated. 6) Steps 4 and 5 are repeated for the other field configuration (IP or OOP). 7) Steps 4-6 are repeated for different temperatures, if needed.

An alternative way is to use field modulation with the Helmholtz coils. In this case, a slightly different experimental setup is needed. Referring again to Figure B.2, the OSC IN port of the lock-in is NOT connected. Instead, the OSC out on the lock-in is connected to the HelmholtZ port on the FMR probe (green line in Figure B.2). Since the oscillator output ports in lock-ins are usually not designed to deliver a large current, but a voltage signal instead, a current amplifier (B.2i) is usually necessary to deliver enough current to the coils (usually around 100-150 mA) to produce an appreciable field to modulate the microwave signal running through the sample. The rest of the experimental setup is similar to the lock-in setup discussed above.

The following steps are followed to measure the FMR response using field modulation: 1) The microwave source power level is selected (as described in the source modulation part above). 2) The first microwave frequency of interest is set in the microwave source. 3) The lock-in is set to internal reference mode. Then, steps 4-7 from the source modulation procedure described above are followed.

B.5 FMR Characterization

FMR occurs when the microwave frequency exciting a sample matches the precession frequency of the electrons within the sample. Here, the electrons are collectively able to absorb the microwave power and their precession angle is maximized. Thus, FMR is detected by looking for a drop in the transmitted power as the external field is swept. The linewidth of the drop, usually measured as the full width at half the maximum drop of the signal, indicates the homogeneity by which the electrons collectively precess. Inhomogeneous linewidth broadening results from impurities and processes such as two-magnon scattering[6]. Therefore, measuring the FMR linewidth can give insight into the purity of a grown sample, as well as its magnetic damping constant. FMR spectroscopy also allows one to extract the effective magnetization of the sample, as well as its gyromagnetic ratio γ. If FMR measurements are performed at different temperatures, it is also possible to extract the Curie temperature as well.

For VNA measurements, the FMR data is plotted as S12 (or S21) versus Frequency. There is a plot for each field measured. Using a lock-in with a field sweep on the other hand, prompts a slightly different plot: the lock-in signal is plotted versus field, and there is a different plot for each microwave frequency used. With the exception of field modulation plot, the FMR plot for either VNA or lock-in can be fitted using the Lorentz + AntiLorentz model[7] with the following fit equations:

$$\begin{aligned}\mathbf{V} = \quad & V_{sym}\frac{\Delta F^2}{(\mathbf{F_0} - F_{res})^2 + \Delta F^2} \\ & + V_{asy}\frac{\Delta F^2(\mathbf{F_0} - \Delta F)}{(\mathbf{F_0} - F_{res})^2 + \Delta F^2} + V_{OS} \qquad \text{(B.2)}\end{aligned}$$

$$\begin{aligned}\mathbf{V} = \quad & V_{sym}\frac{\Delta H^2}{(\mathbf{H_0} - H_{res})^2 + \Delta H^2} \\ & + V_{asy}\frac{\Delta H^2(\mathbf{H_0} - \Delta H)}{(\mathbf{H_0} - H_{res})^2 + \Delta H^2} + V_{OS} \qquad \text{(B.3)}\end{aligned}$$

Where equation B.2 is used for VNA data, and equation B.3 is used for lock-in data. The only difference between the two equations is that the frequencies in

---

[6] M. J. Hurben and C. E. Patton, "Theory of two magnon scattering microwave relaxation and ferromagnetic resonance linewidth in magnetic thin films," *Journal of Applied Physics*, vol. 83, no. 8, pp. 4344–4365, 1998.

[7] E. Montoya, T. McKinnon, A. Zamani, E. Girt, and B. Heinrich, "Broadband ferromagnetic resonance system and methods for ultrathin magnetic films," *Journal of Magnetism and Magnetic Materials*, vol. 356, pp. 12 – 20, 2014.

equation B.2 are swapped for fields in equation B.3. In these equations, V_{sym} and V_{asy} represent the symmetrical and asymmetrical portions of the FMR signal, respectively. ΔF (ΔH) is the frequency (field) linewidth, F_0 (H_0) is the x axis values of the detected VNA (lock-in) signal, F_{res} (H_{res}) is the resonance frequency (field), and V_{OS} is a fit parameter to compensate for any DC offset in the signal.

In the case where field modulation is used, the lock-in measures the change in the power loss with respect to time, i.e. the power derivative, rather than the direct power loss, thus a different equation is needed to extract the resonance fields and linewidths as follows[8]:

$$\mathbf{V} = \frac{\frac{a(H_{res}-\mathbf{H})}{\Delta H} + 9b - 3b(\frac{H_{res}-\mathbf{H}}{\delta H})^2}{(3+(\frac{H_{res}-\mathbf{H}}{\delta H})^2)^2} \tag{B.4}$$

In equation B.4, a and b are fitting parameters, H_{res} is the resonance field, and ΔH is the linewidth.

Extracting the different resonance fields and their frequencies enables one to plot the FMR frequency versus field. These plots are known as dispersion curves and can be fitted with Kittel equations to extract the effective magnetization M_{eff} and the gyromagnetic ratio γ. The Kittel fit equations vary depending on if the field was applied IP or OOP as follows[9]:

$$\mathbf{F_{res}(IP)} = \gamma\sqrt{\mathbf{H_{res}(H_{res} + M_{eff})}} \tag{B.5}$$

$$\mathbf{F_{res}(OOP)} = \gamma(\mathbf{H_{res} - M_{eff}}) \tag{B.6}$$

---

[8] C. J. Oates, F. Y. Ogrin, S. L. Lee, P. C. Riedi, G. M. Smith, and T. Thomson, “High field ferromagnetic resonance measurements of the anisotropy field of longitudinal recording thin-film media,” *Journal of Applied Physics*, vol. 91, no. 3, pp. 1417–1422, 2002.

[9] E. Montoya, T. McKinnon, A. Zamani, E. Girt, and B. Heinrich, “Broadband ferromagnetic resonance system and methods for ultrathin magnetic films,” *Journal of Magnetism and Magnetic Materials*, vol. 356, pp. 12 – 20, 2014.

The g-factor is a unitless variation of γ and can be calculated by simply dividing γ by the *Bohr magneton* which has the value of $1.399\ 624\ 493\ 61 \times 10^{10}$ Hz T^{-1}. The gyromagnetic ratio γ and its corresponding g-factor are especially important characteristics for certain fields such as spintronics. A g-factor of 2 indicates free electrons with no orbital interaction[10], while a g-factor with a value larger than 2 indicates spin-orbit interactions. Spin-orbit interaction, or coupling, gives rise to interesting and useful phenomena such as the Spin Hall Effect (and its inverse)[11] and the Spin Nernst Effect[12]. Further FMR measurements at different temperatures enable the plotting of γ versus temperature, which can reveal interesting properties such as an anisotropic, temperature-dependent g-factor[13]. It also enables the plotting of the effective magnetization versus temperature, which could be fitted with a Bloch function to extract the Curie temperature T_C by using the following equation[14]:

$$\mathbf{M_{eff}} = M_0(1 - (\frac{\mathbf{T}}{T_c})^{\frac{3}{2}}) \tag{B.7}$$

Where M_0 is the effective magnetization at 0 K.

Another plot enabled by the Kittel fits is the linewdith versus frequency. The slope of such plot gives the magnetic damping constant α, as cab be deduced from

---

[10] J. M. Shaw, H. T. Nembach, T. J. Silva, and C. T. Boone, "Precise determination of the spectroscopic g-factor by use of broadband ferromagnetic resonance spectroscopy," *Journal of Applied Physics*, vol. 114, no. 24, p. 243906, 2013.

[11] J. E. Hirsch, "Spin hall effect," *Phys. Rev. Lett.*, vol. 83, pp. 1834–1837, Aug 1999.

[12] S. Meyer, Y.-T. Chen, S. Wimmer, M. Althammer, T. Wimmer, R. Schlitz, S. Geprägs, H. Huebl, D. K ödderitzsch, H. Ebert, G. E. W. Bauer, R. Gross, and S. T. B. Goennenwein, "Observation of the spin nernst effect," *Nature Materials*, vol. 16, pp. 977-981, Oct 2017.

[13] S. Khan, C. W. Zollitsch, D. M. Arroo, H. Cheng, I. Verzhbitskiy, A. Sud, Y. P. Feng, G. Eda, and H. Kurebayashi, "Spin dynamics study in layered van der waals single-crystal cr2ge2te6," *Phys. Rev. B*, vol. 100, p. 134437, Oct 2019.

[14] R. F. L. Evans, D. Hinzke, U. Atxitia, U. Nowak, R. W. Chantrell, and O. Chubykalo-Fesenko, "Stochastic form of the landau-lifshitz-bloch equation," *Phys. Rev. B*, vol. 85, p. 014433, Jan 2012.

the following equation[15]:

$$\mathbf{\Delta H} = \frac{2\alpha}{\sqrt{3} \mid \gamma \mid} \mathbf{F_{res}} + \Delta H_0 \tag{B.8}$$

In equation B.8, H_0 is the linewidth at zero frequency.

---

[15] E. Montoya, T. McKinnon, A. Zamani, E. Girt, and B. Heinrich, "Broadband ferromagnetic resonance system and methods for ultrathin magnetic films," *Journal of Magnetism and Magnetic Materials*, vol. 356, pp. 12 – 20, 2014.

Appendix C

Modified FMR Fitting Procedure

FMR profiles are usually fitted to the superposition of a Lorentzian + anti-Lorentzian functions[1,2] as discussed in Appendix B. The fittings yield the resonance magnetic field and the Full Width at Half Maximum (FWHM) linewidth ΔH_{FWHM}. Then the resonance frequencies f vs. the FMR resonance fields H_{r} are plotted at different temperatures for the IP and OOP field directions as shown in Figure C.1a. Next the procedures described in Ref. [2] is followed to fit the resonance frequency vs. resonance field data points. Because Cu(1,3-bdc) is an easy plane magnet, the standard Kittel equations can be used to fit the data[1,2]:

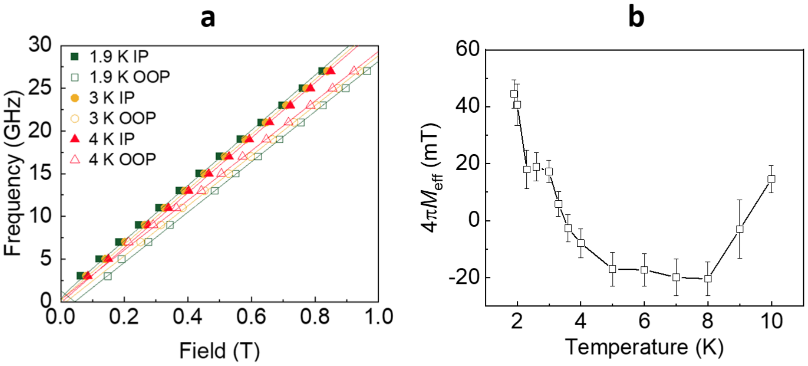

Figure C.1: **a.** Resonance frequency f vs. resonance field H_{r} at 1.9 K, 3 K, and 4 K for external fields applied IP (solid points) and OOP (open points) for Cu(1,3-bdc). The data points were fitted with Equations (C.1) and (C.2). **b.** Temperature dependence of FMR-extracted effective magnetization $4\pi M_{\mathrm{eff}}$.

---

[1] C. Oates, F. Ogrin, S. Lee, P. Riedi, G. Smith, and T. Thomson, "High field ferromagnetic resonance measurements of the anisotropy field of longitudinal recording thin-film media," *Journal of Applied Physics*, vol. 91, pp. 1417–1422,02 2002.

[2] H. Chang, P. Li, W. Zhang, T. Liu, A. Hoffmann, L. Deng, and M. Wu, "Nanometer-thick yttrium iron garnet films with extremely low damping," *IEEE Magnetics Letters*, vol. 5, pp. 1–4, 2014.

$$f = \gamma'_{\mathrm{IP}}\sqrt{(H_r + 4\pi M_{\mathrm{eff}})H_r} \tag{C.1}$$

$$f = \gamma'_{\mathrm{OOP}}(H_r - 4\pi M_{\mathrm{eff}}) \tag{C.2}$$

where Equations (C.1) and (C.2) are standard equations for fitting IP and OOP data points, respectively. Here, f is the microwave frequency, $\gamma' = \frac{\gamma}{2\pi}$ is the reduced gyromagnetic ratio, H_{r} is the resonance field, and $4\pi M_{\mathrm{eff}}$ is the effective magnetization, which is dictated by the magnetocrystalline anisotropy field H_{k}. The fittings can yield γ' and $4\pi M_{\mathrm{eff}}$. As shown in Figure C.1b, $4\pi M_{\mathrm{eff}}$ fluctuates between -20 mT and +50 mT within the tested temperature range (1.9 K to 10 K). To overcome possible influence of H_{k}, one can analyze the data points measured at large magnetic fields to obtain accurate results. In this regard, Equations (C.1) and (C.2) can be re-written as the following:

$$f = \gamma'_{\mathrm{IP}}(H_r + 2\pi H_{\mathrm{eff}}) \tag{C.3}$$

$$f = \gamma'_{\mathrm{OOP}}(H_r - 4\pi H_{\mathrm{eff}}) \tag{C.4}$$

where $H_{\mathrm{r}} >> 4\pi M_{\mathrm{eff}}$. M_{eff} is replaced with H_{eff} in the revised Equations. The revised Equations (C.3) and (C.4) are used for the fitting in Chapter 4, considering H_{r} (≥ 0.4 T) is ≈ 9 times that of the magnetic anisotropy field (≤ 0.04 T). However, we have found that the standard equations (Eq. (C.1) and (C.2)) and the revised equations (Eq. (C.3) and (C.4)) generate the same results for our samples.